Received: 22 April 2024 | Revised: 1 November 2024 | Accepted: 7 November 2024

DOI: 10.1002/jev2.70028

RESEARCH ARTICLE

Fused extracellular vesicles from M_2 macrophages and human umbilical cord mesenchymal stem cells for the targeted regulation of macrophage pyroptosis in periprosthetic osteolysis

Qimeng Liu[1] | **Tianliang Ma**[1,2] | **Zheyu Zhang**[1] | **Jiangyu Nan**[1] | **Guanzhi Liu**[1] | **Yute Yang**[1] | **Yihe Hu**[1] | **Jie Xie**[1]

[1]Department of Orthopedics, The First Affiliated Hospital, Zhejiang University School of Medicine, Hangzhou, China

[2]Department of Orthopedics, Xiangya Hospital, Central South University, Changsha, China

Correspondence
Jie Xie and Yihe Hu, Department of Orthopedics, First Affiliated Hospital, School of Medicine, Zhejiang University, No.79 Qingchun Road, Hangzhou, Zhejiang, 310003, China.
Email: dr_xiejie@zju.edu.cn and xy_huyh@163.com

Funding information
Zhejiang Provincial Natural Science Foundation of China, Grant/Award Number: Y24H060021; National Natural Science Foundation of China, Grant/Award Numbers: 82272452, 82372414, 82202733

Abstract

The development of strategies for the prevention and treatment of aseptic loosening of prostheses stands as a critical area of global research interest. The pyroptosis of local macrophages triggered by wear particles plays a pivotal role in the onset of periprosthetic osteolysis and subsequent loosening. Extracellular vesicles, carrying the surface components and regulatory molecules of their parent cells, embody the cellular characteristics and biological functions of these progenitors. In a pioneering approach to precisely inhibit the pyroptosis of local macrophages induced by wear particles, we have engineered fused extracellular vesicles (fEV) from M_2 macrophages and human umbilical cord mesenchymal stem cells. These fEV boast the distinctive capability for targeted transport and immune evasion, collectively enhancing the anti-pyroptosis effect of the therapeutic extracellular vesicles. Our research demonstrates the targeted, significant preventive and therapeutic potential of fEVs against periprosthetic osteolysis prompted by wear particles, highlighting its crucial clinical significance and application prospects. These findings suggest that extracellular vesicle fusion technology heralds a novel paradigm in the design and development of targeted extracellular vesicle-based drug delivery systems.

KEYWORDS
aseptic loosening, fused extracellular vesicles, macrophage pyroptosis, periprosthetic osteolysis, targeted therapy

1 | INTRODUCTION

As the World's population ages, the demand for joint replacements is rising steadily, leading to significant social and economic challenges. Aseptic prosthesis loosening (APL), a condition where the bone-implant interface becomes loose in the absence of infection, stands as the most critical complication post-joint replacement (Hodges et al., 2021). Data indicates that of 53,150 knee and 92,588 hip replacements, 38.7% and 49.2% of revisions were due to aseptic loosening, respectively (Pan et al., 2023). The genesis of this issue is widely attributed to periprosthetic osteolysis, triggered by wear particles from the artificial joints. Despite its acknowledged impact, the exact mechanisms driving this osteolysis—complicated by factors like metabolic and immune changes, osteoporosis and ageing—remain poorly understood. Consequently, effective clinical interventions to prevent this condition are

Qimeng Liu and Tianliang Ma contributed equally to this study.

scarce, leaving joint revision as the sole alternative (Dong et al., 2022). In essence, aseptic loosening significantly undermines the long-term success of joint prostheses, representing a pressing clinical challenge that demands immediate attention.

Understanding the formation of wear particles and the pathological mechanisms underlying osteolysis following artificial joint replacement is crucial for preventing and treating APL. Identified wear debris particles include polyethylene, bone cement and metal particles such as titanium (Ti), cobalt, chromium and molybdenum. These particles, often resulting from long-term friction between the prosthesis and bone tissue or among various prosthesis components, are typically micron or nano-sized. Accumulating around the prosthesis, these particles incite an immune phagocytic overload reaction (Drees et al., 2007). The wear particles induce a sterile inflammatory response in the body, prompting macrophages to release pro-inflammatory factors like interleukin-1β (IL-1β), interleukin-18 (IL-18) and tumour necrosis factor-alpha (TNF-α). This process activates the Receptor activator of the nuclear factor kappa B (RANK) signalling pathway, leading to osteoclast activation and local osteolysis around the prostheses (Cobelli et al., 2011; Goodman & Gallo, 2019). Specifically, the binding of RANK Ligand (RANKL) to RANK on osteoclast progenitor cells activates nuclear factor kappa B (NF-κB) through a series of molecular interactions. This activation stimulates the expression of genes critical for osteoclast formation, such as the nuclear factor of activated T cells cytoplasmic 1 (NFATc1), resulting in osteoclast differentiation and formation (An et al., 2018). The excessive osteoclast activity leads to osteolysis near the prosthesis and the host bone, contributing to APL (Edwards & Mundy, 2011). In essence, the inflammatory response triggered by wear particles forms the primary pathological basis of APL. However, further research is needed to fully elucidate the pathological mechanisms and identify molecular targets beyond the inflammatory response induced by wear particles.

Research suggests that direct downstream cytological events triggered by wear particles in vivo have not been extensively studied. Macrophages, key cells involved in bone resorption on the periosteal surface, are stimulated by repeated phagocytosis of wear particles. This stimulation leads to the production of pro-inflammatory mediators and proteolytic enzymes, with wear particle-induced bone resorption being a primary cause of periprosthetic osteolysis (Drees et al., 2007). One notable pathway involves the activation of the NOD-like receptor protein 3 (NLRP3) inflammasome in macrophages by wear particles, which then promotes osteolysis through the NLRP3/caspase-1/IL-1β pyroptosis signalling pathway (Tschopp & Schroder, 2010). The NLRP3 inflammasome is comprised of a sensor (NLRP3), an adaptor (apoptosis-associated speck-like protein, ASC), and an effector (caspase-1) (Wu et al., 2022c). Activation of this inflammasome leads to caspase-1 activation, which in turn promotes the release of the gasdermin D (GSDMD) fragment, GSDMD-NT. This fragment is involved in cell membrane perforation, facilitating the release of IL-1β, and inducing cell pyroptosis (Conos et al., 2017; Zhu et al., 2017). IL-1β is recognized as a key cytokine in the pathological cascade of prosthesis aseptic loosening, driving a positive feedback loop of pyroptosis-osteolysis-pyroptosis, ultimately leading to osteolysis (Kim et al., 2009).IL-1β, released during macrophage pyroptosis, promotes osteoclast generation through the RANK-RANKL axis, significantly enhancing bone resorption (Son et al., 2020a). Additionally, IL-1β activates the NLRP3 inflammasome through various pathways, including the direct activation by ATP and potassium ions released due to cell injury and necrosis. The IL-1β-mediated opening of the pannexin 1 pore allows wear particles to directly interact with NLRP3, further stimulating its activation (Burton et al., 2013; Tschopp & Schroder, 2010). Despite these insights, current research has not yet fully explored the precise mechanisms by which the inhibition of wear particle-induced periprosthetic macrophage pyroptosis could mitigate periprosthetic osteolysis.

Human umbilical mesenchymal stem cells (hucMSC) play a crucial role in tissue repair predominantly through paracrine signalling pathways (Wei et al., 2023). Small extracellular vesicles (sEV) derived from hucMSC (hucMSC-EV) serve as a principal mechanism for their paracrine effects. Specifically, hucMSC-EVs carrying miR-378a-5p have been shown to inhibit the NLRP3 inflammasome, mitigating macrophage pyroptosis and consequently preventing dextran sulfate sodium-induced colitis (Cai et al., 2021). Moreover, hucMSC-EV can alleviate inflammatory pain via the miR-146a-5p/tumour necrosis factor receptor-associated factor 6 (TRAF6) pathway, enhancing autophagy levels while inhibiting pyroptosis (Hua et al., 2022). Additionally, hucMSC-EV down-regulates miR-421 expression, further inhibiting pyroptosis and reducing the release of pro-inflammatory cytokines IL-1β and IL-18 (Yan et al., 2020). This evidence underscores the potential of hucMSC-EV as protective agents against pyroptosis, suggesting their theoretical viability in curbing periprosthetic macrophage pyroptosis induced by wear particles. However, challenges remain in achieving targeted delivery of hucMSC-EV to areas of periprosthetic osteolysis and maintaining effective therapeutic concentrations.

sEV stands as prime candidates for drug delivery, leveraging their phospholipid bilayer structure as the foundation for liposome-like drug delivery systems (He et al., 2018). These systems facilitate enhanced drug accumulation in targeted areas, alongside improved stability and circulation time for small-molecule drugs (Kim et al., 2016; Saari et al., 2015). Being nanoscale vesicles secreted by cells, sEV carries the surface components and regulatory molecules of their parent cells, embodying the cellular traits and biological functions of the originating cells (Rayamajhi et al., 2019). sEV derived from M_2 macrophages (M_2-EV) are particularly effective for delivering drugs to areas of inflammation. They naturally possess the macrophages' innate ability to chemotactically navigate toward inflammatory sites and the capability to avoid clearance by the reticuloendothelial system (RES) and immune detection. This enables them to effectively target and accumulate drugs in regions of chronic inflammation (Tang et al., 2018). In the context of combating periprosthetic osteolysis, we propose using M_2-EV for the targeted delivery of hucMSC-

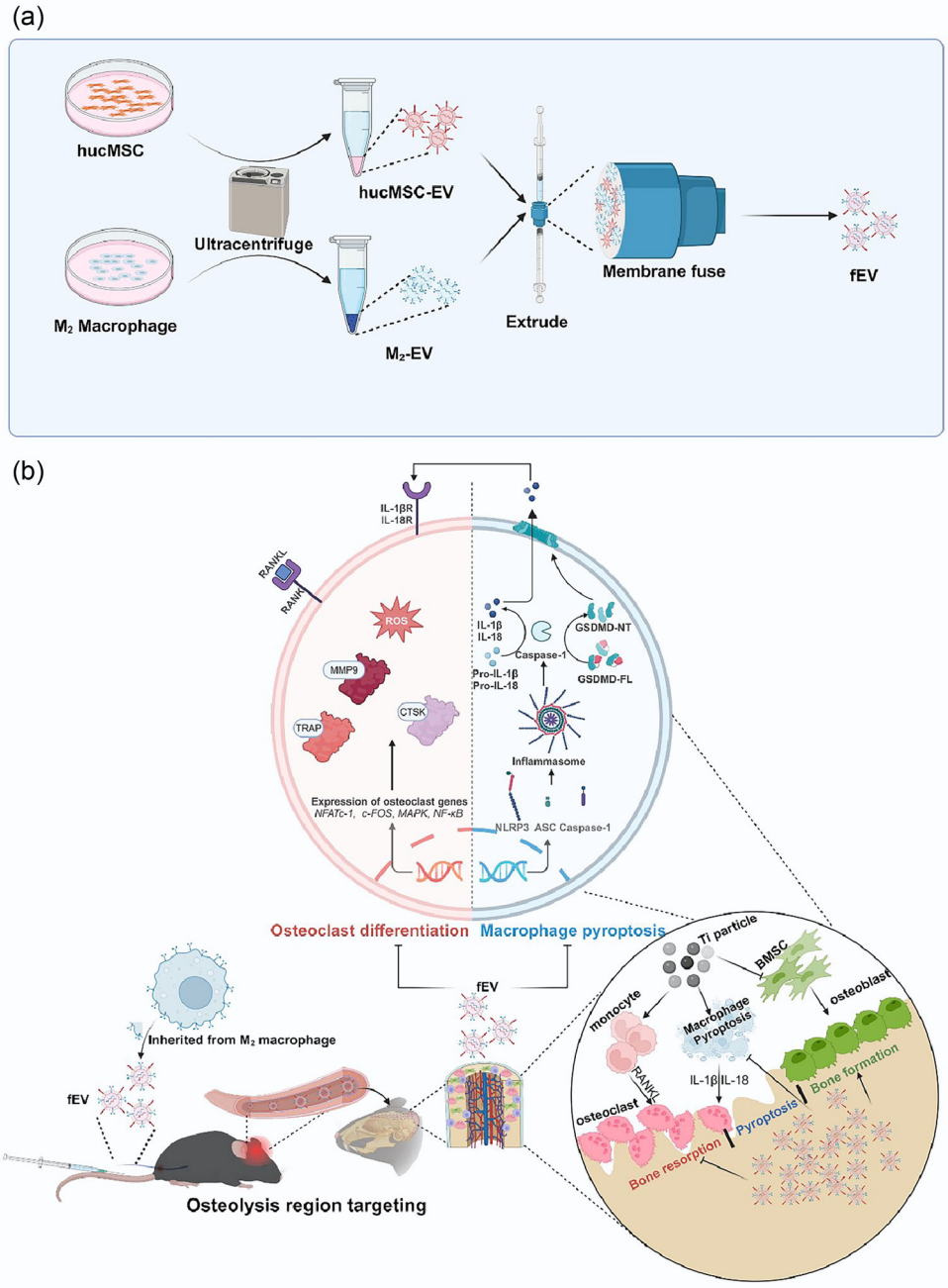

SCHEME 1 (a) Schematic diagram of fEV as a potential candidate to treat periprosthetic osteolysis. (b) Schematic diagram of mechanism of fEV on periprosthetic osteolysis. Created in BioRender. Zhou, Y. (2024) https://BioRender.com/v68o867

EV to the affected areas around prostheses. This approach is grounded on several principles: (1) The local aseptic inflammation induced by wear particles around the prosthesis sets the stage for the chemotactic targeting by M_2-EV (Panez-Toro et al., 2023). (2) Based on the phospholipid bilayer structure, membrane fusion technologies (Dehaini et al., 2017; Huang et al., 2023), membrane encapsulation EV (Hu et al., 2021; Li et al., 2022b) and EV-liposome fusion (Li et al., 2022a; Wu et al., 2023) provide the technical backbone for facilitating EV fusion. (3) M_2-EV incorporates macrophage membrane proteins for directed chemotaxis to inflammatory regions and contains regulatory molecules that can suppress cell pyroptosis (Dai et al., 2020; Tang et al., 2022). For the first time, this study proposes and constructs fusion extracellular vesicles (fEV) combining M_2-EV and hucMSC-EV for precise, targeted therapeutic delivery in the periprosthetic osteolysis region. The fEV aims to accurately inhibit macrophage pyroptosis at the site, offering a novel strategy for the prevention and treatment of periprosthetic osteolysis (Scheme 1).

2 | MATERIALS AND METHODS

2.1 | Study approval

The research protocol involving human tissue specimens was approved by the Clinical Research Ethics Committee of the First Affiliated Hospital of Zhejiang University School of Medicine, with informed consent obtained from all donors. Animal experimentation procedures adhered strictly to protocols approved by the Experimental Animal Ethics Committee of the First Affiliated Hospital of Zhejiang University School of Medicine. Throughout the experiment, mice were housed in a specific pathogen-free (SPF) environment, maintaining a temperature range of 22°C–24°C, humidity levels between 45% and 55%, and subjected to a consistent 12-h light/dark cycle.

2.2 | H&E staining and histomorphometric analysis

The human synovial tissue and the peripheral boundary membrane tissue of the human prosthesis were fixed in 4% paraformaldehyde (PFA, Servicebio, China) for 24 h, while the mouse skull was decalcified in ethylenediamine tetraacetic acid (EDTA, Servicebio, China) (0.5 M, pH 7.2) for a week. Subsequently, the tissues were embedded in paraffin and sectioned. Following staining with hematoxylin (Servicebio, China), counterstaining with eosin (Servicebio, China), and mounting with neutral gum (Servicebio, China), the sections were scanned using a pathological section scanner to assess histological changes and inflammatory cell infiltration. Image J software was employed for the analysis of periosteal membrane thickness.

2.3 | Immunohistochemical and immunofluorescent staining

The paraffin sections were subjected to dewaxing using xylene, followed by rehydration. Subsequently, they were treated with a 3% H_2O_2 methanol solution at room temperature for 20 min to block non-specific staining. Antigen retrieval was performed using the pressure cooker method, with the appropriate antigen retrieval solution chosen based on the antibody instructions. To prepare for immunohistochemical staining, the sections were enclosed in a 5% bovine serum albumin (BSA, Servicebio, China) solution at room temperature for 1 h. They were then incubated overnight at 4°C with primary antibodies targeting GSDMD (Abcam, UK), IL-1β (Abcam, UK), and runt-related transcription factor-2 (RUNX2, Abcam, UK). The following day, the sections were removed from 4°C and allowed to warm up for 10–20 min. For immunohistochemical staining, secondary antibodies labelled with horseradish peroxidase (Abcam, UK) were applied and incubated at room temperature for 1 h. Nuclei were restained after DAB colour development at room temperature, followed by sealing with neutral gum tablets. The sealed slides were air-dried in a ventilated cupboard and then scanned using a pathological section scanner. For immunofluorescence staining, the corresponding fluorescent secondary antibody (Abcam, UK) was incubated at room temperature for 1 h. The nuclei were stained with DAPI (Biosharp, China), and the slides were sealed. The images were observed and captured using a fluorescence microscope (Leica, Germany). Image J software was utilized to analyse the positive regions and fluorescence intensity.

2.4 | Cell lines and conditions

The methods described in the literature were followed to isolate mouse bone marrow-derived macrophages (BMDM) (Weischenfeldt & Porse, 2008), hucMSC (Dong et al., 2018), and human bone marrow mesenchymal stem cells (hBMSC) (Chen et al., 2021). RAW 264.7 cells were procured from the American Type Culture Collection (ATCC, Manassas, VA, USA). BMDM were cultured in RPMI 1640 medium (BioChannel Biological Technology Co., Ltd.) with 10% fetal bovine serum (FBS, Umedium HeFei China) supplemented with macrophage colony-stimulating factor (M-CSF, R&D Systems, USA) (20 ng/mL), while hucMSC were cultured in a specialized stem cell culture medium (OriCell, China). hBMSC and RAW 264.7 cells were cultured in the DMEM medium (CYTOCH) with 10% FBS (JYK-FBS-301, INNER MONGOLIA JIN YUAN KANG BIOTECHNOLOGY CO., LTD.), and cryopreserved with cell freezing medium (HAKATA, China). All cell cultures were maintained at 37°C in a humidified atmosphere with 5% CO_2.

2.5 | sEV isolation

The polarization of BMDM to M_2 macrophages was induced by 20 ng/mL of interleukin-4 (IL-4, R&D Systems, USA) and 10 ng/mL of interleukin-13 (IL-13, R&D Systems, USA) and identified by surface marker F4/80 (BD, USA), CD206 (BD, USA) by

flow cytometry LongCyteTM (Challenbio, China) (Ying et al., 2021). M_2 macrophages or hucMSC were separately seeded in 10 cm dishes (NEST, China) at the density of 8×10^6 cells/dish and cultured in the complete medium supplemented with EV-free serum (Umibio [Shanghai] Co., Ltd.) for 48 h, and the supernatants were collected for the isolation and identification of extracellular vesicles. sEVs were isolated through a process of differential centrifugation (Ying et al., 2017). Initially, the cell medium was centrifuged at 500 × *g* at 4°C for 10 min to remove live cells. The resulting supernatant underwent a subsequent centrifugation step at 2000 × *g* at 4°C for 10 min to eliminate cell debris. Afterwards, the supernatant was subjected to centrifugation at 12,000 × *g* at 4°C for 20 min to remove organelles. Following this, the centrifuged supernatant was filtered using a 0.22 μm filter (Jet Biofil) and subsequently centrifuged at 100,000 × *g* at 4°C for 70 min. Any soluble protein contaminants were eliminated through washing and precipitation with 50 mL of phosphate-buffered saline (PBS, HAKATA, China). Finally, the precipitate obtained after centrifugation at 100,000 × *g* at 4°C for 70 min constituted the purified sEVs, the BCA protein quantification kit (New Cell & Molecular Biotech, China) is used to determine the protein concentration of sEVs. It is feasible to quantitatively detect the protein expression between different Extracellular Vesicles derived from different cells with a nanoflow cytometer referring to the previous studies (Chen et al., 2024; Yim et al., 2023). We applied this assay to detect the expression of hucMSC specific-proteins (CD29, CD73 and CD90) (BD, USA) and M_2-specific proteins (CD206, F4/80) (BD, USA).

2.6 | Preparation of fEV

Various ratios of M_2-EV and hucMSC-EV were blended in a 5% polyethylene glycol solution. Ultrasonic treatment was applied to facilitate the fusion of EVs, whereby the mixture underwent ultrasonic processing for 5 min (5 s–0 s–5 s) using an ultrasonic cleaning device (Yu clean, China) with 40 kHz frequency and 80 W power. Subsequently, the fEV was produced by extruding through the LiposoFast LF1 liposome extruder (Avestin, Canada). Briefly, the mixed EV solution was sucked into the syringe. After connecting to the Luer taper, push back and forth the syringe piston to pass the solution through the 100, 50 nm porous polycarbonate film for 20 times. The sample was transferred into ultrafiltration tubes (10 kDa, Millipore, USA) and centrifuged at 10,000 rpm for 10 min at 4°C, washed with PBS and resuspended with PBS.

2.7 | Flow cytometry

The lipophilic dyes DiI (Beyotime, China) and DiO (Beyotime, China) were prepared as instructed. DiI was utilized to label M_2-EV, while DiO was used to label hucMSC-EV. Following labelling, the samples were incubated at room temperature for 30 min away from light. Subsequently, the DiI-labelled M_2-EV and DiO-labelled hucMSC-EV were transferred into 0.5 mL ultrafiltration tubes (10 kDa, Millipore, USA) and centrifuged at 10,000 rpm for 10 min at 4°C. The resulting ultrafiltrate was washed with PBS and centrifuged again. Different protein ratios of M_2-EV to hucMSC-EV (3:1, 2:1, 1:1, 1:2, 1:3) were mixed to prepare the fEV. The VSSC mode of flow cytometry was employed to identify fEV, with corresponding collection parameters (PE, FITC) being set. The proportion of PE^+FITC^+ nanoparticles was calculated using FlowJo software.

2.8 | Western blotting analysis

EVs or cell samples were lysed using RIPA buffer (Biodragon, AbBox, China) and quantified using a BCA protein quantification kit. Subsequently, 30 μg of protein was separated via sodium dodecyl sulfate-polyacrylamide gel electrophoresis (SDS-PAGE, SurePAGE™, GenScript) and transferred onto a PVDF membrane (Millipore, USA). The membrane was blocked with 5% BSA at room temperature for 1 h, followed by three washes with TBST (Servicebio, China). The PVDF membrane was then incubated overnight at 4°C with primary antibodies against Calnexin (Abcam, UK), CD63 (Abcam, UK), TSG101 (Abcam, UK), caspase-1 (Abcam, UK), cleaved caspase-1 (Cell Signaling Technology, USA), GSDMD (Abcam, UK), cleaved GSDMD (Cell Signaling Technology, USA), IL-1β (Abcam, UK), cleaved IL-1β (Cell Signaling Technology, USA), ASC (Abcam, UK), RUNX2 (Abcam, UK), Osterix (Abcam, UK) and α-tubulin (Abcam, UK). After washing with TBST, the PVDF membrane was incubated with the corresponding horseradish peroxidase-conjugated secondary antibody (Abcam, UK) at room temperature for 1 h. Following another round of washing with TBST, Robust ECL Solution (Swiss Affinibody LifeScience AG) and the ECL Prime Western Blotting system was used to visualize the expected protein bands. Image Lab software was utilized for protein quantitative analysis.

2.9 | Coomassie blue staining

The EVs were lysed using RIPA buffer and quantified using a BCA protein quantification kit. Subsequently, 30 μg of protein was isolated via SDS-PAGE. After carefully removing the gel, any excess gel was trimmed off, and Coomassie blue dye (Beyotime,

China) was added to cover the gel completely. The gel was then incubated on a room temperature shaker for 1–2 h. Following the incubation period, the dyeing solution was discarded, and the gel was washed thoroughly with double-distilled water until the wash solution no longer exhibited a blue colour. Finally, the gel was removed and photographed for analysis.

2.10 | Colocalization analysis

RAW264.7 cells were cultured to a density of 75%–85%. Subsequently, 2×10^4 RAW264.7 cells were seeded into a glass bottom cell culture dish (NEST Biotechnology, China) and incubated overnight in a cell incubator. M_2-EV was labelled with the lipophilic dye DiI, while hucMSC-EV was labelled with the lipophilic dye DiO. Following labelling, M_2-EV and hucMSC-EV were either mixed or utilized to prepare fEV. RAW264.7 cells were then treated with 100 μg of either mixed EV or fEV and incubated in a cell incubator for 4 h in the absence of light. After removing the culture medium, the cells were washed with PBS and fixed with 4% paraformaldehyde for 10 min. Subsequently, the cells were washed again with double-distilled water, and a ready-to-use DAPI staining solution was added, followed by incubation at room temperature for 10 min. The positioning relationship between the green DiO signal, red DiI signal and blue DAPI signal (indicating the nucleus) was observed using a confocal laser scanning microscope. The co-positioning coefficient was calculated and analysed using Image J software.

2.11 | Co-immunoprecipitation analysis

Protein samples were extracted from lysed cells, and the decoy protein ASC was precipitated using magnetic bead-coupled antibodies specific to ASC. Following precipitation, the protein complexes were separated via SDS-PAGE, and the presence of the target protein caspase-1 was detected through Western blotting analysis. To ensure the reliability of the results and verify natural interactions, both positive and negative control groups were established. The positive control group (Input) confirmed the presence of both ASC and caspase-1, validating the experimental setup. Conversely, the negative control group (IgG) was implemented to eliminate the possibility of nonspecific binding between proteins and antibodies, thus ensuring the specificity of the observed interactions.

2.12 | ELISA

5×10^5 BMDM were seeded into the well plates and cultured in the incubator. Following a 3 h treatment with 100 ng/mL lipopolysaccharide (LPS, Sigma, USA), the cells were subsequently exposed to 0.1 mg/mL Ti particles (Aladdin, China). Experimental groups received additional treatment with 300 μg/mL of hucMSC-EV, M_2-EV, mixed EV and fEV based on the initial intervention. After 9 h of treatment, the supernatant was collected for analysis. Using ELISA kits (R&D systems, Minnesota, USA) according to manufacturer instructions, the expression levels of IL-1β and IL-18 in the cell supernatant were measured to assess the impact of the interventions.

2.13 | Live and dead staining

After treatment of Ti with or without EVs, the supernatant was replaced with a live/dead staining solution (Beyotime, China). Subsequently, cells were incubated in darkness at 37°C for 30 min. Fluorescent images of live/dead cells were captured by the confocal laser scanning microscope and analysed using Image J software.

2.14 | LDH release assay

After treatment of Ti with or without EVs, the supernatant was collected for analysis according to the manufacturer's recommended protocol. Briefly, the percentage of LDH release was calculated with the following formula: $(LDH_s - LDH_b)/(LDH_{max} - LDH_b) \times 100\%$. LDH_s, LDH_b, LDH_{max}, are the OD490 values measured for the supernatant treated by the LDH activity assay kit (Solarbio, China), the untreated medium and the cell lysis solution.

2.15 | Osteoclast differentiation

5×10^4 cells of BMDM were seeded into each well of a 48-well plate (Jet Biofil, China). Upon cell adhesion to the surface, they were subjected to an osteoclast induction medium containing 100 ng/mL RANKL (R&D systems, Minnesota, USA).

The experimental groups were treated with 300 μg/mL of hucMSC-EV, M_2-EV, mixed EV and fEV. The culture medium was replenished every 2 days. Once osteoclasts reached maturity, they were fixed with 4% paraformaldehyde for 10 min and subsequently washed with PBS. Following the manufacturer's instructions, a tartrate-resistant acid phosphatase (TRAP, Sigma, USA) staining solution was prepared and applied to the cells. Incubation at 37°C, shielded from light, was carried out until the osteoclasts exhibited a distinct purple-red coloration. The number of osteoclasts was then observed and analysed under an inverted microscope. Additionally, the expression levels of osteoclast differentiation-related mRNAs and proteins were analysed using western blotting and qRT-PCR assay.

2.16 | ROS assay

According to the manufacturer's recommended protocol of the reactive oxygen species (ROS) staining kit (Beyotime, China). 5×10^4 cells of BMDM were seeded into each well of a 48-well plate (Jet Biofil, China). Upon cell adhesion to the surface, they were subjected to an osteoclast induction medium containing 100 ng/mL RANKL (R&D systems, Minnesota, USA). The experimental groups were treated with 300 μg/mL of hucMSC-EV, M_2-EV, mixed EV and fEV. After 48 h, each group was then incubated with DCFH-DA (Beyotime, China) at 37°C for 1 h. A confocal laser scanning microscope was used to detect ROS levels.

2.17 | qRT-PCR

Total RNA extraction kit (New Cell & Molecular Biotech, China) and Evo M-MLV reverse transcriptase kit (ACCURATE BIOTECHNOLOGY(HUNAN) CO., LTD, Changsha, China) were used for RNA extraction and cDNA synthesis. qRT-PCR was performed using SYBR Green (APExBIO, Houston, USA) with gene-specific primers. After normalized by *β-Actin*, gene expression was calculated by $2^{-\Delta\Delta Ct}$. Primer sequences used in this study were listed in Table S1.

2.18 | Osteogenic differentiation

Primary hBMSC were seeded into 48-well plates at a density of 5×10^4 cells per well and cultured overnight in a cell incubator. The control group was subjected to an osteogenic induction solution (OriCell, China) to initiate osteogenic differentiation, while the experimental group received intervention with 100 μg/mL of hucMSC-EV, M_2-EV, mixed EV and fEV. Following 7 days of intervention, the cells were subjected to alkaline phosphatase (ALP, Beyotime, China), alizarin Red S (ARS, OriCell, China) and sirius red staining (Solarbio, China), followed by quantitative analysis. Additionally, the expression levels of osteogenic differentiation-related proteins, namely RUNX2 and Osterix, were analysed using a western blotting analysis.

2.19 | Calvarial osteolysis models

Male C57BL/6J mice ($n = 5$ per group) aged 8–10 weeks were anesthetized via intraperitoneal injection of pentobarbital (50 mg/kg). Following the incision of the skull skin along the midline, the periosteum covering the skull surface was carefully removed. Subsequently, 30 mg of titanium (Ti) wear particles were applied to the exposed skull surface, and the incision was closed using 4-0 prolene sutures.

2.20 | In vivo imaging system

The cranial osteolysis model was established in male C57BL/6J mice ($n = 3$ per group) aged 8–10 weeks. One day post-modelling, hucMSC-EV, M_2-EV, mixed EV and fEV (100 μL, 200 μg) labelled with DiR (Yeasen, China) were administered via tail vein injection. Subsequently, fluorescence imaging using IVIS was conducted at 12, 24, 36, 48 and 60 h post-injection to track the distribution of the administered fEV. The fluorescence intensity in the skull region was analysed at each time point. After 60 h, the skulls and major organs of the mice were harvested, and the distribution of fEV in the skull and major organs was analysed to assess their biodistribution.

2.21 | Micro-computer tomography (Micro-CT) analysis

Bone scans were conducted using Micro-CT with the following scanning parameters: 50 kV, 500 μA, and a resolution of 6.5 μm. Following reconstruction, regions of interest (ROI) were carefully delineated to measure parameters including the bone surface/bone volume (BS/BV), bone volume /total volume (BV/TV) and total porosity.

2.22 | Statistical analysis

All data in this study were collected in triplicate except for specific notation. Experimental results were statistically analysed and presented as mean ± standard deviation. Statistical analyses were conducted using GraphPad Prism 9, Image J and Image Lab software. The mean of two groups of data was compared using an independent sample *t*-test, while a one-way analysis of variance (ANOVA) was employed to compare the means of multiple groups of data. A *P*-value less than 0.05 was considered statistically significant, with "ns" indicating no statistically significant difference. Additionally, the symbols "$^{*}P < 0.05$, $^{**}P < 0.01$, $^{***}P < 0.001$" denoted statistical significance at the corresponding levels.

3 | RESULTS

3.1 | Pathological characteristics of the periprosthetic membrane

To explore the pathological characteristics of the periprosthetic boundary membrane in patients with periprosthetic osteolysis, synovial membrane (SM) tissue was collected from patients undergoing primary total hip replacement due to femoral neck fracture, while periprosthetic membrane (PM) was obtained from patients experiencing aseptic hip prosthesis loosening resulting in periprosthetic osteolysis. Histological examination with H&E staining revealed distinct differences in cell composition and morphological features between SM and PM tissues. PM tissue exhibited disordered tissue structure with evident inflammatory cell infiltration, indicative of pathological changes associated with periprosthetic osteolysis (Figure 1a). Furthermore, we investigated the expression levels of pyroptosis-related proteins in PM tissue to assess the extent of pyroptosis. Immunohistochemical analysis revealed significantly higher expression of the pyroptosis executive protein GSDMD in the inflammatory regions of PM tissue compared to SM tissue (Figure 1b,d). Additionally, the IL-1β-positive area in PM tissue was approximately 15 times greater than that in SM tissue ($P < 0.001$), indicating a heightened release of pyroptosis-associated factors in PM tissue (Figure 1c,e). These findings underscore the inflammatory milieu and pyroptosis as prominent pathological features of PM tissue, potentially contributing to the inflammation and pathological bone resorption triggered by wear particles.

3.2 | The preparation and characterization of identification of fEV

sEVs have emerged as promising vehicles for drug delivery, offering efficient transport of diverse cargo. Here, we present a novel approach for the targeted delivery of therapeutic EVs to the periprosthetic osteolysis region through the construction of fEV derived from M_2-EV and hucMSC-EV. To obtain M_2 macrophages, BMDM was fully induced with IL-4 (20 ng/mL) and IL-13 (10 ng/mL) for 48 h. The expression level of the M_2 macrophage marker CD206 significantly increased post-induction, as confirmed by a loss of cells assay (Figure S1). Subsequently, the supernatants of M_2 macrophages and hucMSC cultures were collected, and EVs were isolated using an ultra-high-speed centrifugation method for fEV construction. We initially assessed the fusion efficiency of fEV prepared with varying initial proportions of M_2-EV and hucMSC-EV. M_2-EV were labelled with DiI, while hucMSC-EV were labelled with DiO. Flow cytometry analysis (VSSC mode) revealed a notably higher proportion of double-positive particles in the fusion sample (fEV) compared to the mixed sample (mixed EV). Remarkably, the highest ratio of double positivity was observed when the initial ratio of M_2-EV to hucMSC-EV was 1:1 (Figure 2a,b). Consequently, we utilized a 1:1 ratio of M_2-EV to hucMSC-EV for fEV preparation in subsequent studies. Transmission electron microscopy (TEM) observation demonstrated that while EVs exhibited saucer-like vesicles, fEV exhibited distinct and intact disk-like vesicles (Figure 2c). The average particle size of EV ranged between 100–120 nm, whereas the particle size of fEV prepared via ultrasound combined with adiposome extruder was more uniform, approximately 50 nm. Additionally, the average zeta potential between EV and fEV was approximately −11 mV (Figure 2d). Western blotting analysis confirmed the expression of characteristic sEV proteins CD63 and TSG101 in both M_2-EV, hucMSC-EV and fEV, while the endoplasmic reticulum protein Calnexin was not detected, indicating that fEV retained typical sEV properties (Figure 2e). Flow cytometry analysis (VSSC mode) revealed that hucMSC-specific proteins are specifically enriched in hucMSC-EV, M_2 macrophage-specific proteins are specifically enriched in M2-EV, while proteins all above are enriched in fEV (Figure S8a,b). Coomassie blue staining further revealed that fEV retained the protein expression profiles of both M_2-EV and hucMSC-EV, affirming the preservation of their protein composition during fEV preparation (Figure S2). The fusion of fEV was directly visualized using laser confocal scanning microscopy. Confocal images demonstrated that while the green and red signals remained separated in the mixed EV group, fluorescence signals in the fEV group were well-co-located (Figure 2f,g). In summary, fEV derived from M_2-EV and hucMSC-EV were successfully prepared using ultrasound combined with a liposome extrusion instrument, while preserving the biological characteristics of both parental sEVs.

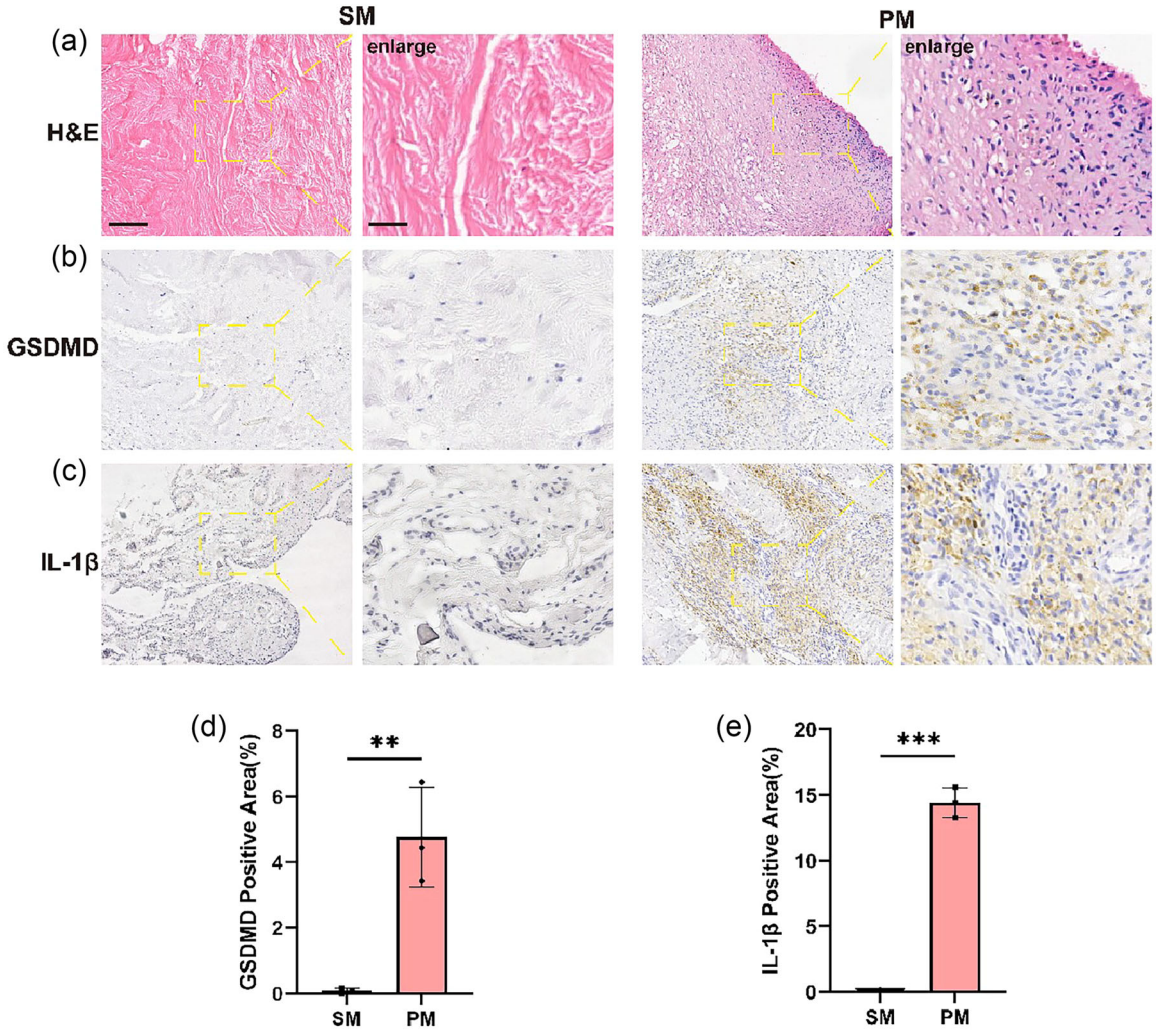

FIGURE 1 Pathological characteristics of the periprosthetic membrane. (a) H&E staining of SM and PM. Immunohistochemical analysis of (b) GSDMD (c) IL-1β (d, e) relative quantitation of GSDMD positive area (%) and IL-1β positive area (%) (scale bar, 100 μm, 30 μm [enlarged]. The data in the figures represent the averages ± SD, $n = 3$ samples per group, $^{*}P < 0.05$, $^{**}P < 0.01$, $^{***}P < 0.001$).

3.3 | fEV inhibited macrophage pyroptosis in vitro

We initially investigated the impact of fEV on macrophage pyroptosis in vitro. A CCK-8 (Shandong Sparkjade Biotechnology Co., Ltd.) assay demonstrated that fEV did not exhibit any significant cytotoxicity or adverse effects on macrophages (Figure S3). Live and dead staining and lactate dehydrogenase (LDH) release assay results revealed that Ti particles markedly induced cell death in BMDM following LPS pre-treatment, whereas fEV and mixed EV notably reversed this phenomenon. However, the individual effects of M_2-EV and hucMSC-EV alone were not significant (Figure 3a,e and Figure S4a). ASC oligomerization, speck formation and assembly serve as initiation signals for pyroptosis. Interestingly, fEV and mixed EV intervention significantly attenuated the speck formation of ASC aggregation and assembly induced by LPS+Ti particles (Figure 3b,f). Western blotting analysis revealed that compared to M_2-EV or hucMSC-EV intervention alone, fEV and mixed EV intervention reduced the levels of pyroptosis regulatory molecules in cell lysates. Specifically, lower expression levels of caspase-1 p20, GSDMD-NT and IL-1β p17 were observed (Figure 3c and Figure S4b–d). Further insights were obtained through co-immunoprecipitation, which visually demonstrated the impact of fEV on the binding of ASC and caspase-1 during inflammasome assembly. Notably, fEV exhibited the least binding of ASC-caspase1 in comparison to the mixed EV group, resulting in the lowest level of cell pyroptosis. Subsequent analysis of pyroptosis-related factors in the cell supernatant revealed that LPS+TI intervention led to heightened levels of IL-1β and IL-18, indicative of increased cell pyroptosis. Treatment with M_2-EV and hucMSC-EV individually mitigated this process, with fEV and mixed EV exhibiting the most pronounced effects. Overall, these findings underscore the potent inhibitory effect of fEV on macrophage pyroptosis in vitro.

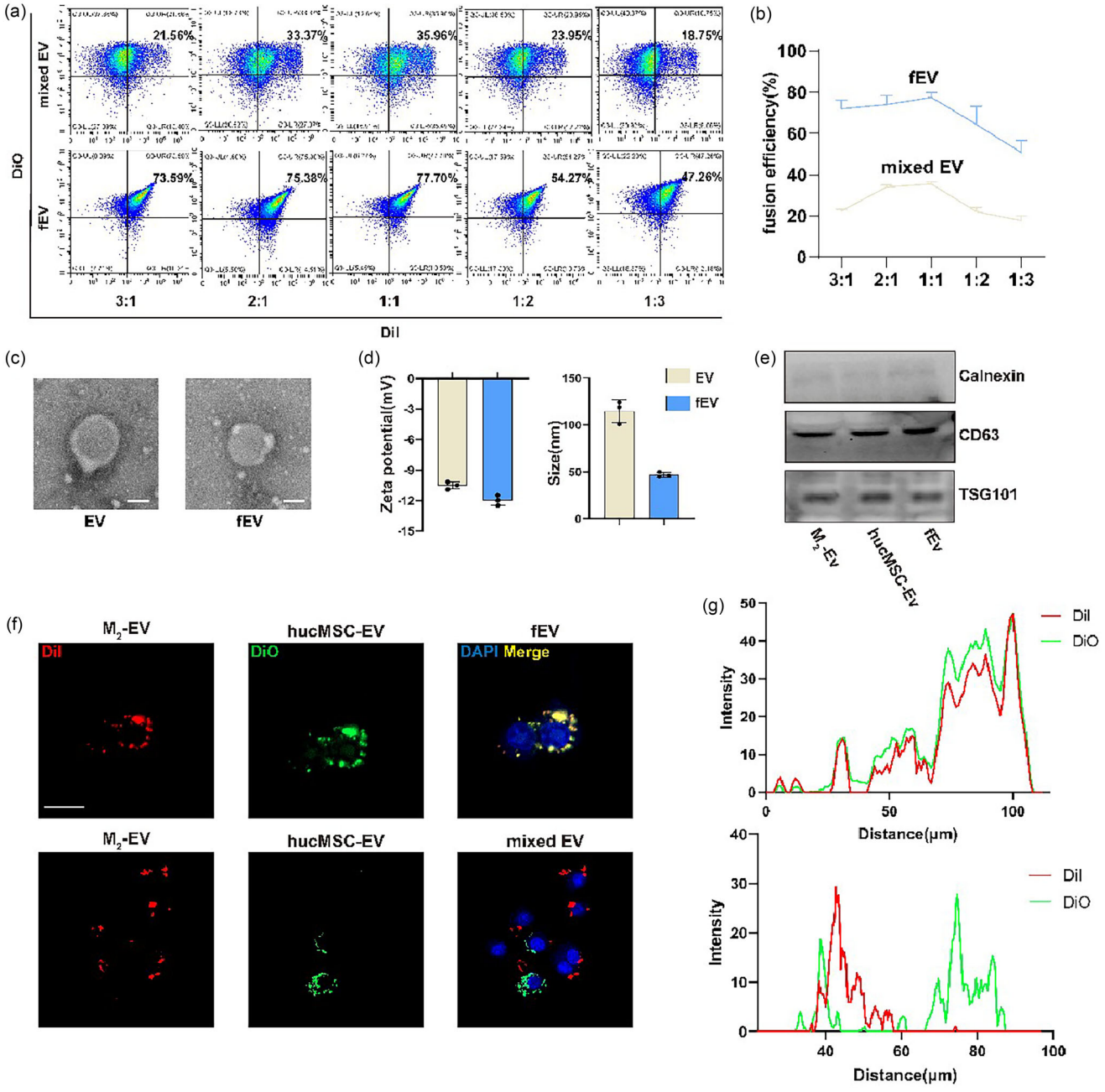

FIGURE 2 The preparation and characterization of identification of fEV. (a, b) Fusion ratio of EVs analysed by flow cytometry (VSSC mode) (c) TEM images of EV and fEV. Scale bar, 50 nm (d) Zeta potential and average size of EV and fEV. (e) The marker of EV was analysed by western blotting. (f) Typical confocal images and (g) co-localization analysis of RAW264.7 incubated with fEV and mixed EV. Scale bar, 10 μm. DiI (red) labelled M_2-EV, DiO (green) labelled hucMSC-EV before fused or mixed.

3.4 | fEV inhibited osteoclastic differentiation of macrophages and promoted osteogenic differentiation in vitro

To explore the impact of fEV on the osteoclastic differentiation of macrophages, we initially examined its effect on RANKL-induced macrophage ROS production. Remarkably, we observed a significant reduction in ROS fluorescence intensity in the fEV group compared to the individual M_2-EV or hucMSC-EV groups, indicative of a pronounced inhibition of osteoclast differentiation signalling (Lee et al., 2005). Subsequently, we directly assessed the effect of fEV on osteoclast formation through TRAP staining. As illustrated in Figure 4b,e, both fEV and mixed EV effectively decreased the number of osteoclasts, surpassing the efficacy of the M_2-EV or hucMSC-EV groups. Moreover, we investigated the impact of fEV on the podosome arrangement of osteoclasts. While osteoclasts in the RANKL-induced group displayed a distinct actin-formed podosome band, those treated

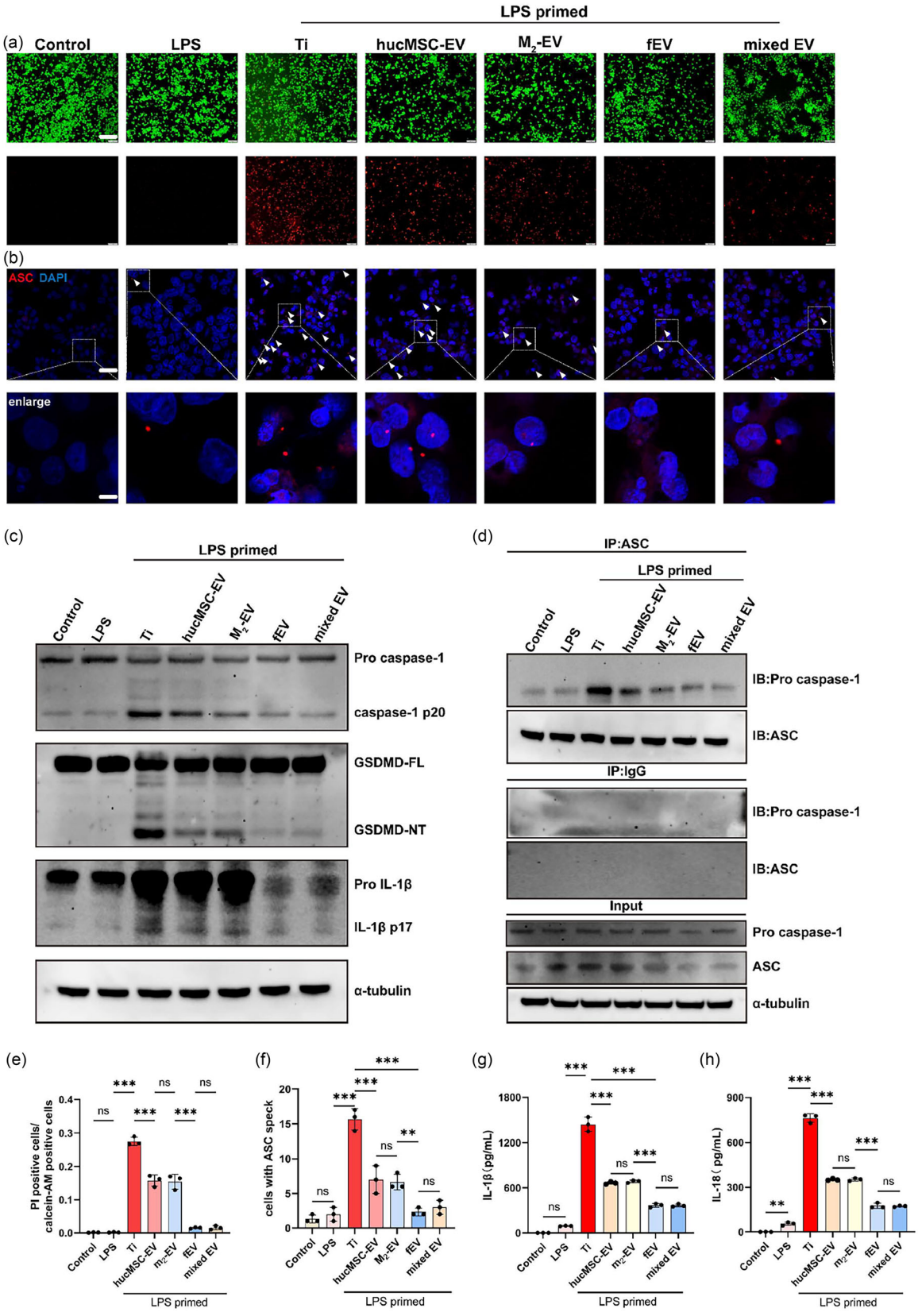

FIGURE 3 fEV inhibited macrophage pyroptosis in vitro. (a) Live and dead staining images and quantification (e) of BMDM (LPS and Ti induced) treated with EV. Scale bar, 100 μm. (b) Immunofluorescence images and quantification (f) of ASC speck formation in BMDM (LPS and Ti induced) treated with EV (ASC specks were labelled by white arrow). Scale bar, 50 μm, 10 μm (enlarged). (c) Pyroptosis-related protein analysed by western blotting. (d) Binding of ASC and caspase-1 in BMDM (LPS and Ti induced) treated with EV. (g) IL-1β and (h) IL-18 in the cell supernatant analysed by ELISA (the data in the figures represent the averages ± SD, $n = 3$ samples per group, $^{*}P < 0.05$, $^{**}P < 0.01$, $^{***}P < 0.001$).

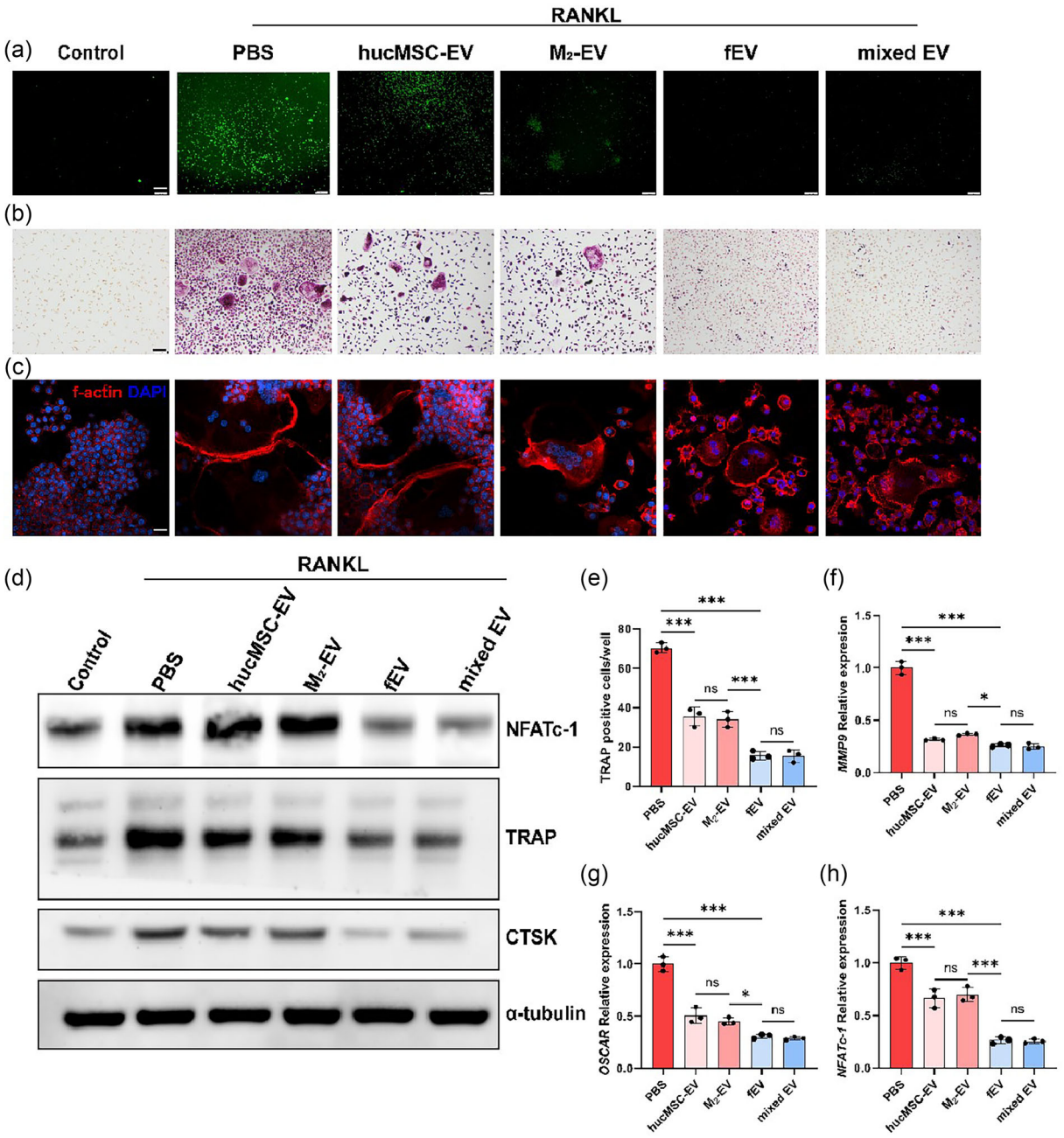

FIGURE 4 fEV inhibited osteoclastic differentiation of macrophages in vitro. (a) The ROS (green) production was assayed using a fluorescence microscope. Scale bar, 100 μm. (b) Osteoclast differentiation of BMDM (RANKL induced) was analysed by TRAP staining and (e) its quantification. Scale bar, 50 μm. (c) Phalloidin labelled F-actin in osteoclasts. Scale bar, 100 μm. (d) Osteoclast-related protein and mRNA were analysed by western blotting and (f–h) qRT-PCR (the data in the figures represent the averages ± SD, $n = 3$ samples per group, $^{*}P < 0.05$, $^{**}P < 0.01$, $^{***}P < 0.001$).

with fEV and mixed EV exhibited scattered podosomes (Figure 4c). Western blotting experiments further revealed that fEV notably suppressed the expression levels of NFATc-1, TRAP, and Cathepsin-K (CTSK) proteins (Figure 4d and Figure S5a–c). Additionally, qRT-PCR analysis demonstrated that fEV down-regulated the mRNA expression levels of MMP9, OSCAR and NFATc-1 (Figure 4f–g). Collectively, these findings indicate that fEV effectively inhibits the differentiation and maturation of macrophages into osteoclasts in vitro.

To explore the effects of fEV on the osteogenic differentiation of hBMSC, we assessed its impact on ALP expression, calcium nodule formation, and collagen deposition during hBMSC osteogenesis using ALP, ARS, and sirius red staining, respectively. As anticipated, both M_2-EV and hucMSC-EV contributed to ALP expression, calcium nodule formation, and collagen deposition during hBMSC osteogenic differentiation to some extent. However, treatment with fEV and mixed EV further augmented these effects (Figure 5a–c). Quantitative analysis of the corresponding eluents after ARS and Sirius red staining corroborated these

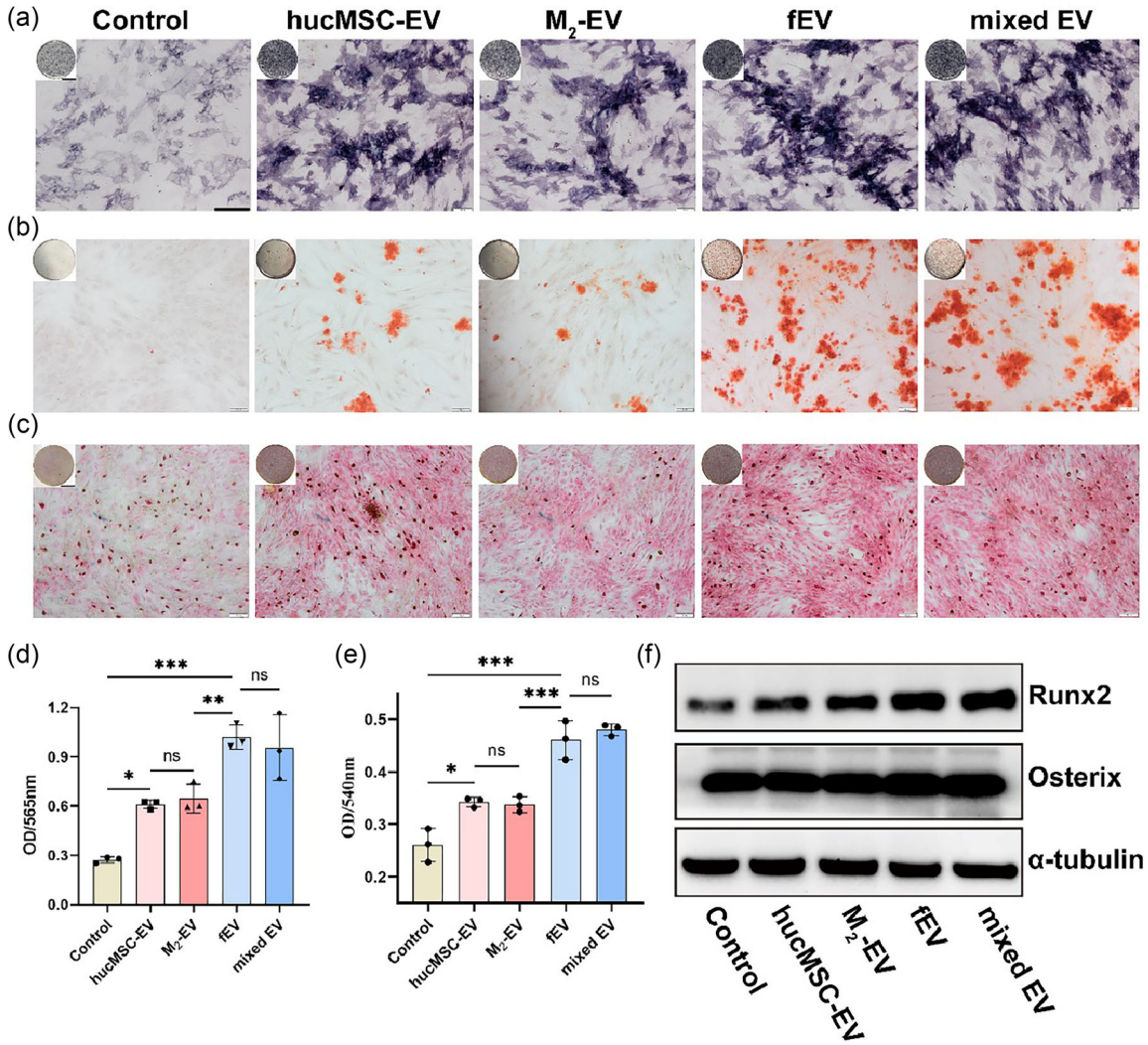

FIGURE 5 fEV promoted osteogenic differentiation in vitro. ALP expression, calcium nodule formation, and collagen deposition during hBMSC osteogenesis were treated with EV using (a) ALP, (b) ARS and (c) sirius red staining. Scale bar, 400 μm, 100 μm (enlarged). (d, e) Quantitative analysis of the corresponding eluents after ARS and sirius red staining. (f) Osteogenic-related protein of hBMSC analysed by western blotting (the data in the figures represent the averages ± SD, $n = 3$ samples per group, $^{*}P < 0.05$, $^{**}P < 0.01$, $^{***}P < 0.001$).

findings (Figure 5d,e). Additionally, Western blotting analysis of RUNX2 and Osterix protein expression levels during hBMSC osteogenic differentiation revealed that the fEV and mixed EV groups exhibited superior promotion of osteogenic differentiation compared to the M_2-EV or HucMSC-EV groups (Figure 5f and Figure S6). In summary, these results demonstrate that fEV promotes the osteogenic differentiation of hBMSC in vitro.

3.5 | The targeting of fEV to the osteolysis area around the prosthesis

To explore the in vivo application potential of fEV, we investigated its ability to target the osteolysis area around the prosthesis using a mouse cranial osteolysis model induced by Ti particles. In this study, we labelled fEV with the membrane fluorescent dye DiR and employed IVIS for in vivo fluorescence imaging. As depicted in Figure 6a, fluorescence images were captured and fluorescence intensity in the skull region was analysed at various time points (12, 24, 36, 48 and 60 h) following caudal vein injection. The DiR group served as a negative control, eliminating the influence of the DiR dye itself. The hucMSC-EV group exhibited only a low-intensity fluorescence signal in the osteolysis region. Notably, the fluorescence signal peaked at 24 h, with the fEV and M_2-EV groups displaying approximately three times the fluorescence intensity of the hucMSC-EV group ($P < 0.001$) and approximately 2.2 times that of the mixed EV group ($P < 0.001$). These results suggest that EV fusion, rather than simple mixing, significantly enhanced the enrichment level of hucMSC-EV in the osteolysis region. After 60 h, the mice were euthanized,

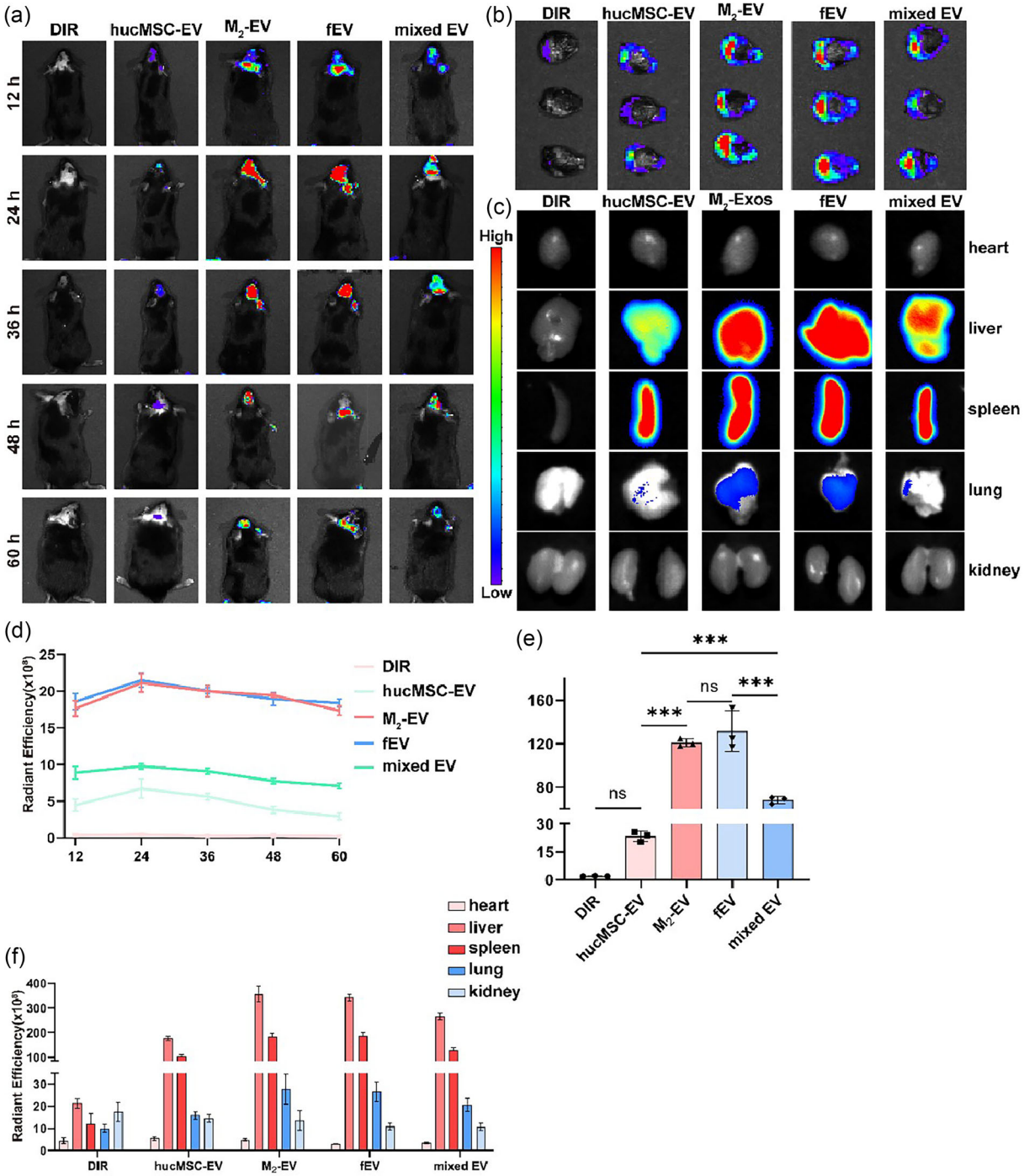

FIGURE 6 The targeting of fEV to the periprosthetic osteolysis. (a) The IVIS images and quantification of the fluorescent intensity (d) after intravenous injections of DiR-labelled hucMSC-EV (200 μg), M_2-EV (200 μg), hucMSC-EV (100 μg) + M_2-EV (100 μg) and fEV (fused with hucMSC-EV (100 μg) + M_2-EV (100 μg)). (b) The EV distribution of the calvarial region, (c) major organ of the mouse and (e, f) their quantification of fluorescent intensity (the data in the figures represent the averages ± SD, $n = 3$ samples per group, $^*P < 0.05$, $^{**}P < 0.01$, $^{***}P < 0.001$).

and skull pieces were extracted for direct quantification of fluorescence intensity in the osteolysis region (Figure 6b). Consistent with the quantitative fluorescence results obtained in vivo, the fluorescence intensity of the fEV and M_2-EV groups in the modelling region was approximately five times that of the hucMSC-EV group and approximately 2 times that of the mixed EV group ($P < 0.001$). Further analysis of fEV distribution in the main organs of the body revealed residual high fEV fluorescence signals in the liver and spleen, indicating that fEV reduced the clearance rate of EV in the body and extended the circulation time to a certain extent. These findings suggest that fEV inherits M_2-EV's significant targeting ability for the osteolytic region and prolongs the circulation time of EV in vivo.

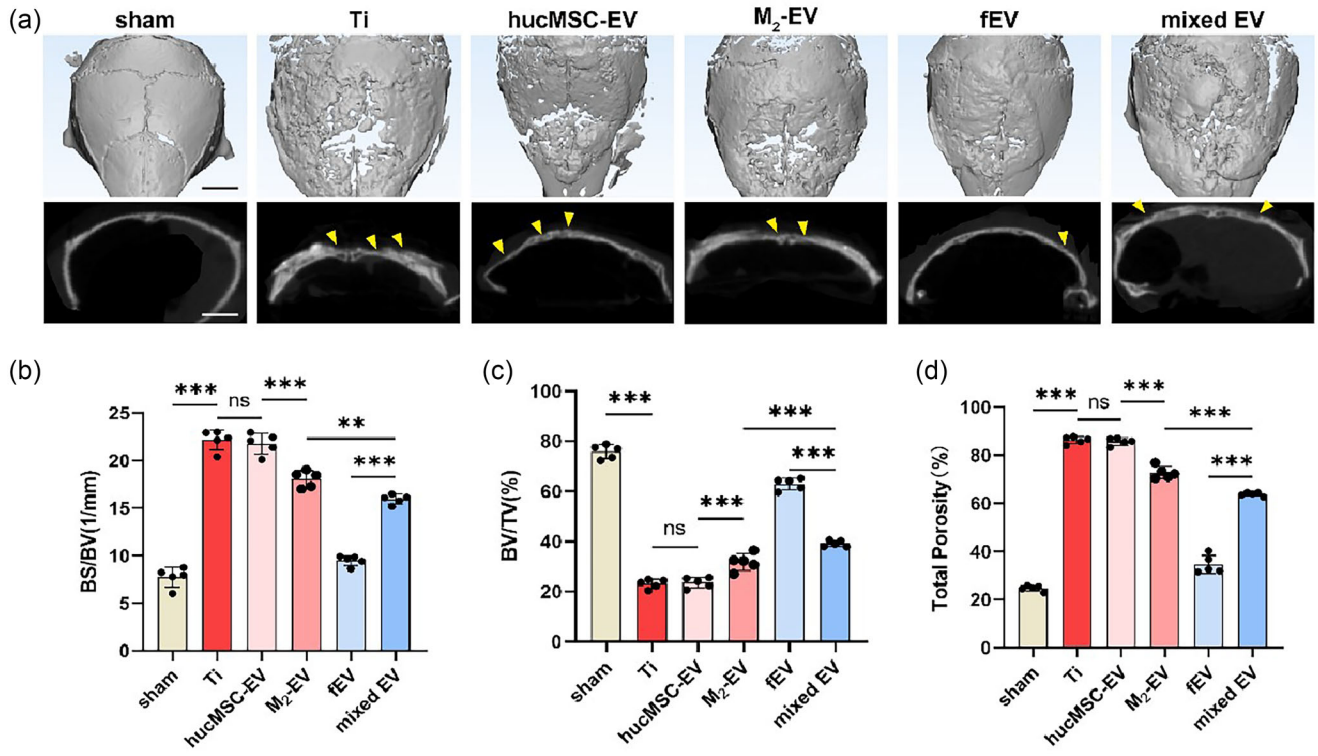

FIGURE 7 Prevention and treatment effect of fEV on periprosthetic osteolysis. CT scan of calvaria sections after intravenous injections of PBS, hucMSC-EV (200 μg), M_2-EV (200 μg), hucMSC-EV (200 μg) + M_2-EV (200 μg) and fEV (fused with hucMSC-EV (200 μg) + M_2-EV (200 μg)) once a week for 5 weeks. (a) 3D reconstruction of Micro-CT was performed (osteolytic lesions were labelled by yellow arrow). Scale bar, 5 mm. (b–d) The quantitative analysis of BS/BV, BV/TV, and total porosity (the data in the figures represent the averages ± SD, $n = 5$ samples per group, $^*P < 0.05$, $^{**}P < 0.01$, $^{***}P < 0.001$).

3.6 | Prevention and treatment effect of fEV on periprosthetic osteolysis

We examined the preventive effect of fEV on periprosthetic osteolysis in vivo. H&E staining of major organs demonstrated the safety profile of fEV in vivo (Figure S7). Micro-CT results (Figure 7a) revealed that, compared to the sham group, the Ti particle group exhibited decreased BV/TV, increased BS/BV, and increased total porosity, indicative of evident osteolytic lesions. The hucMSC-EV group showed limited efficacy due to the lack of targeting to the osteolysis region, while the M_2-EV group demonstrated some therapeutic effects. In contrast, the fEV group, benefiting from both targeted and therapeutic effects, exerted a pronounced inhibitory effect on osteolysis. H&E staining depicted inflammatory cell infiltration in the skull region induced by Ti particles, alterations in normal bone tissue morphology, and increased thickness of inflammatory periosteum. However, fEV intervention restored normal bone tissue morphology and reduced inflammation levels. TRAP staining illustrated that fEV significantly suppressed osteoclast formation in the Ti particle-induced osteolysis region, leading to a substantial reduction in bone resorption activity (Figure 8). Furthermore, fEV's positive impact on osteogenic capacity in the osteolysis region was corroborated, aligning with the in vitro findings. Immunofluorescence analysis demonstrated that fEV enhanced the expression of RUNX2, a protein associated with osteogenic differentiation. These findings collectively suggest that fEV targeting effectively curbs osteolytic lesions in the osteolysis region while promoting bone formation and repair.

3.7 | fEV targeted inhibition of macrophage pyroptosis in the periprosthetic osteolysis

Finally, we investigated the impact of fEV on macrophage pyroptosis levels in the Ti particles-induced osteolysis region in vivo, while also assessing the expression levels of the pyroptotic executive protein GSDMD and the pyroptotic factor IL-1β in the osteolysis region (Figure 9). Immunofluorescence analysis revealed that the expressions of GSDMD and IL-1β in the osteolysis region were significantly upregulated upon Ti particles treatment. However, compared to the fEV group, M_2-EV or hucMSC-EV alone failed to reverse this process due to their lack of therapeutic efficacy or targeting ability. In comparison with the mixed EV group, the fEV group exhibited a marked reduction in the expression of GSDMD and IL-1β induced by Ti particles, indicating a superior capacity for macrophage regulation. These findings underscore the ability of fEV targeting to mitigate the pyroptosis level of macrophages in the osteolysis region induced by Ti particles.

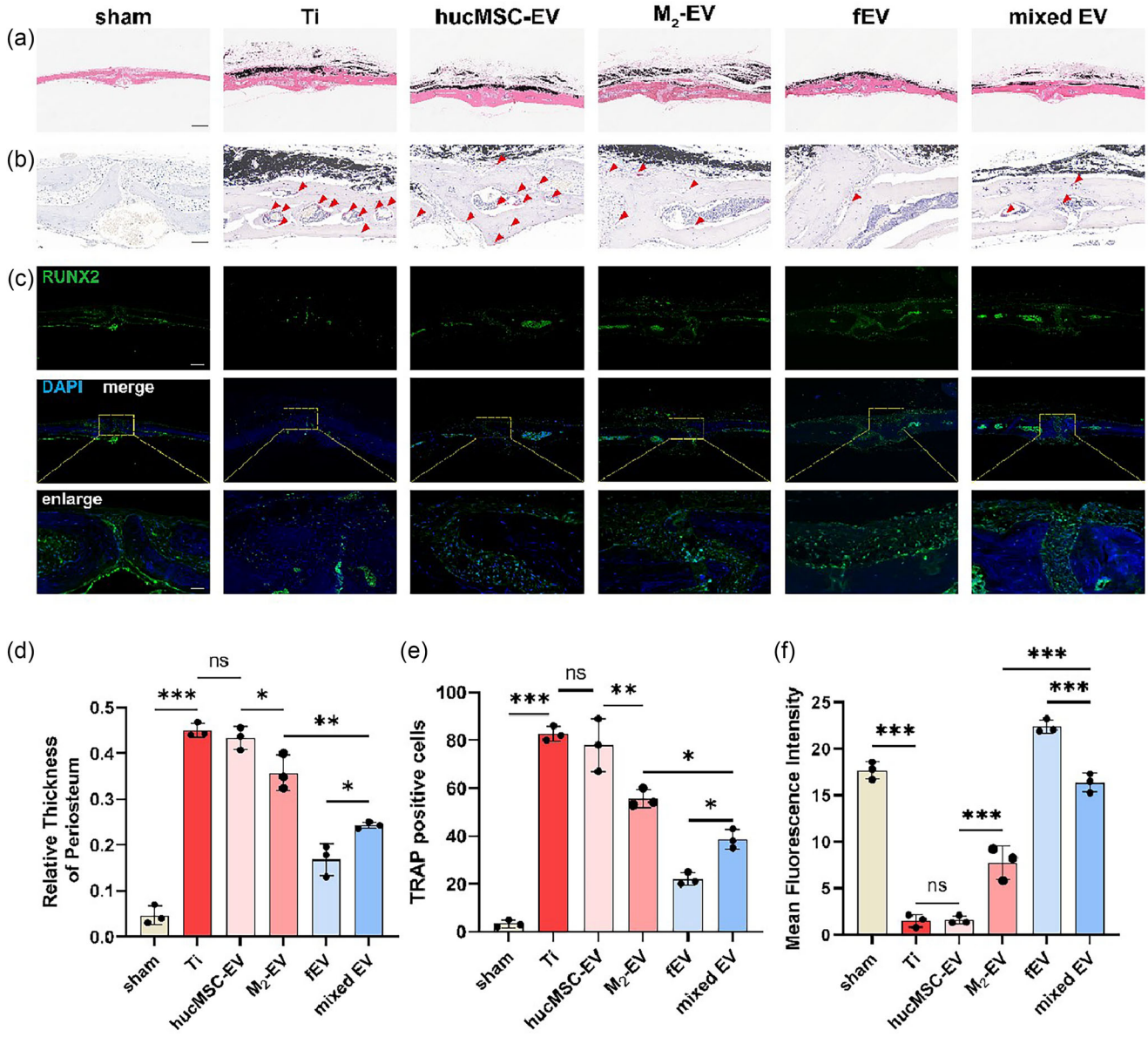

FIGURE 8 Prevention and treatment effect of fEV on periprosthetic osteolysis. (a) H&E staining of calvaria sections and (d) thickness of inflammatory periosteum. Scale bar, 250 μm. (b) TRAP staining of calvaria sections (TRAP positive cells were labelled by red arrow) and (e) the quantifications of TRAP positive cells. Scale bar, 50 μm. (c) Osteogenic related protein RUNX2 was analysed by immunofluorescence and (f) the quantifications of fluorescence intensity. Scale bar, 100 μm, 20 μm (enlarged) (the data in the figures represent the averages ± SD, $n = 3$ samples per group, $^{*}P < 0.05$, $^{**}P < 0.01$, $^{***}P < 0.001$).

4 | DISCUSSION

Periprosthetic osteolysis is characterized by the formation of pathological PM. This process involves mechanical abrasion resulting from the minute relative motion between the prosthesis and bone, leading to bone tissue fragmentation and absorption. Consequently, pathological fibrous tissue, known as the PM, fills the area surrounding the prosthesis (Szmukler-Moncler et al., 1998). Additionally, aseptic inflammation triggered by wear particles around the prosthesis promotes the recruitment of immune cells, fostering the development of chronic granulomatous inflammation and the subsequent formation of pathological PM (Alhasan et al., 2022). The PM tissues create a chronic inflammatory milieu detrimental to bone metabolism, thus fostering macrophage osteoclastic differentiation and bone resorption, ultimately exacerbating joint prosthesis instability (Cobelli et al., 2011). Mitigating PM-related inflammation holds promise as a strategy for preventing and treating aseptic loosening, constituting a core mechanism for restoring periprosthetic tissue homeostasis (Buckley et al., 2014; Fullerton & Gilroy, 2016).

Macrophages play a pivotal role in inducing osteolysis around the prosthesis due to wear particles. Previous studies suggest that macrophage pyroptosis induced by wear particles contributes to periprosthetic osteolysis and subsequent prosthetic loos-

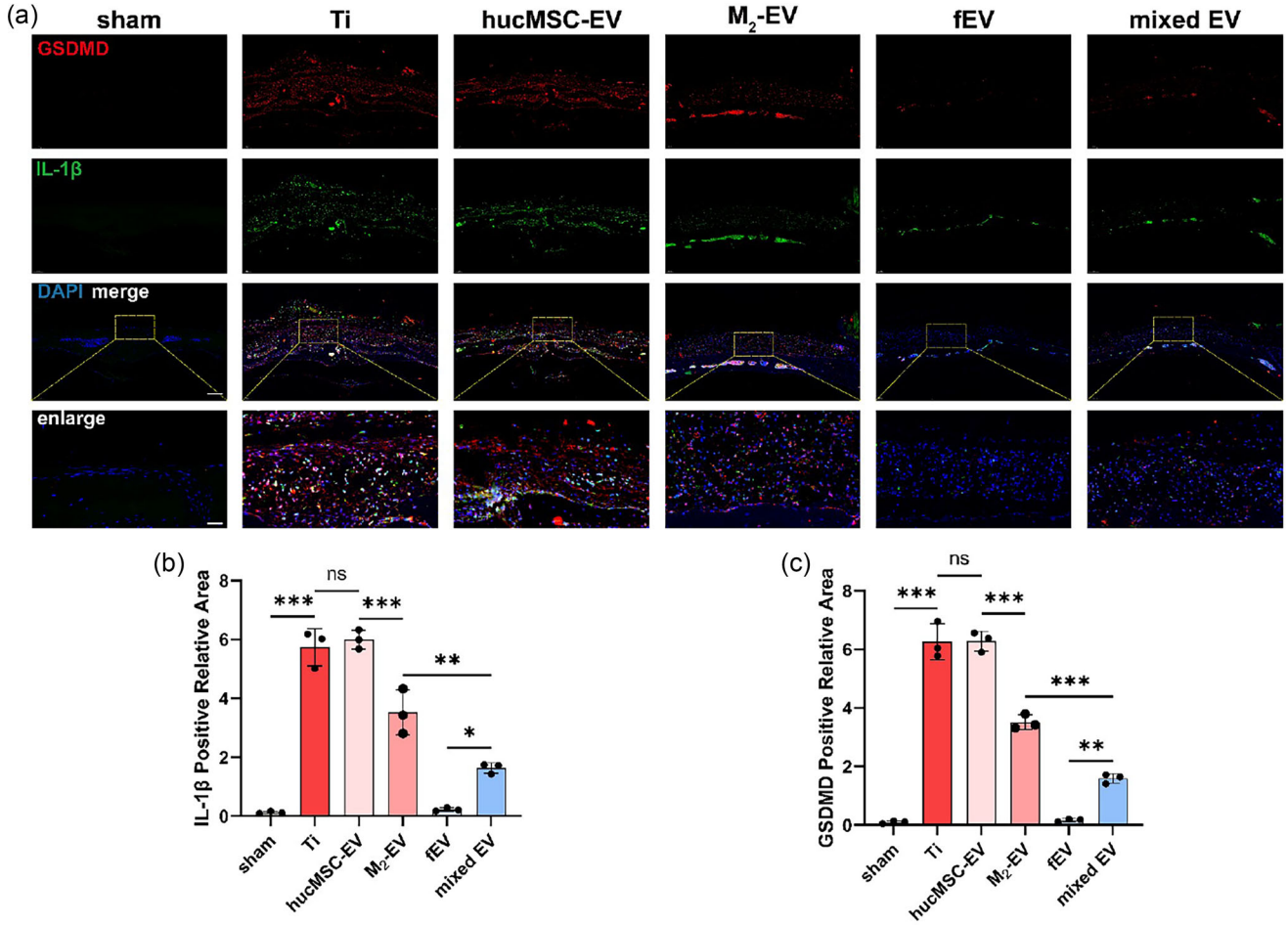

FIGURE 9 fEV targeted inhibition of macrophage pyroptosis in the periprosthetic osteolysis analysed by immunofluorescence images. (a) immunofluorescence staining of pyroptosis-related proteins GSDMD and IL-1β and (b, c) their quantifications (scale bar, 100 μm, 20 μm (enlarged). The data in the figures represent the averages ± SD, $n = 3$ samples per group, $^{*}P < 0.05$, $^{**}P < 0.01$, $^{***}P < 0.001$).

ening following artificial joint replacement (Gallo et al., 2014; Wu et al., 2022a). However, the pathological characteristics of macrophages in PM tissues during periprosthetic osteolysis remain unclear. In light of these scientific inquiries, histological examination via H&E staining has revealed that PM exhibits disorganized tissue structure, unclear hierarchy and infiltration of a large number of inflammatory cells. Immunohistochemical experiments have further confirmed the pyroptotic characteristics of macrophages in PM. This inflammatory response triggers the release of the cytokine IL-1β, which promotes the recruitment and differentiation of osteoclast precursors, leading to increased bone resorption (Son et al., 2020b). Additionally, elevated levels of inflammatory cytokines inhibit the osteogenic differentiation of BMSC and stimulate programmed osteoblast death (Shi et al., 2014; Yin et al., 2020). In conclusion, the inflammatory response triggered by macrophage pyroptosis significantly impacts the balance between bone resorption and osteogenesis. Targeted inhibition of local macrophage pyroptosis around the prosthesis holds promise as an effective strategy for preventing and treating periprosthetic osteolysis.

sEVs serve as crucial mediators for stem cells to exert paracrine effects, with previous research confirming the significant role of hucMSC-EV in regulating macrophage pyroptosis and bone metabolism (Cai et al., 2021; Wang et al., 2020). Leveraging the macrophage pyroptosis regulatory effect of hucMSC-EV, along with employing techniques to evade immune clearance and precisely target the osteolysis area, represents an imperative clinical treatment approach. sEVs, as proficient carriers within biomimetic drug delivery systems, hold substantial promise for disease prevention and treatment. Our previous study demonstrated that macrophage membrane-encapsulated human urine-derived stem cell extracellular vesicles (MM-EV) are targeted therapy for peri-prosthetic osteolysis. However, due to MM's lack of therapeutic effect, taking cues from the inflammation targeting capacity of macrophage (Tang et al., 2018), and drawing from techniques in biofilm fusion and EV-liposome fusion methods, we have successfully engineered an osteolytic region-targeted drug delivery system (fEV). This system utilizes M_2-EV as the carrier for delivering hucMSC-EV as the cargo. A series of experiments have underscored the distinctive capability of fEV in targeted prevention and treatment of prosthesis osteolysis.

Natural cell membranes possess a plethora of functions inherent to their parent cells, including "self" labelling, biological targeting and interaction with the immune system (Wang et al., 2019). When enveloping nanoparticles, cell membranes endow them with certain biological functions, such as prolonged circulation, targeted recognition, enhanced accumulation at disease sites and deep penetration into tumours (Wu et al., 2022b). The inflammatory region-targeting capability of fEV is closely tied to its sustained circulation in vivo and the macrophage cell membrane components inherited from M_2-EV. Previous research has validated that nanoparticles coated with macrophage cell membranes exhibit high efficiency in targeted delivery and demonstrate therapeutic efficacy against various inflammatory conditions (Cao et al., 2016; Li et al., 2019). Cell adhesion molecules, present on the cell surface, mediate interactions between cells and/or the extracellular matrix (ECM). The inflammatory chemotactic properties of macrophages are associated with the expression of cell membrane proteins such as P-selectin, glycoprotein ligand 1 (PSGL-1), L-selectin, lymphocyte function-associated antigen 1 (LFA-1), RGD-binding integrin and macrophage 1 antigen (Wu et al., 2022b; Zaveri et al., 2017). Unlike neutrophils, which have a short lifespan, the prolonged survival of macrophages, spanning several months or even longer, likely contributes to the enduring circulation of nanoparticles coated with macrophage cell membranes (Wynn et al., 2013).

fEV presents as a vesicle-like structure with a diameter of approximately 50 nm, preserving the therapeutic components of both M_2-EV and hucMSC-EV, thereby exerting a regulatory effect on inhibiting macrophage pyroptosis and maintaining bone metabolic homeostasis. MicroRNAs (miRNAs) are small endogenous RNAs that serve as the primary pathway through which sEV exerts post-transcriptional negative regulation of gene expression (Lu & Rothenberg, 2018). It is evident that fEV may directly promote bone formation and inhibit bone resorption through various mechanisms to prevent and treat osteolysis. M_2-EV enhances the osteogenic activity of osteoblasts by targeting olfactomedin-like 1 (OLFML1) with miR-365-2-5 (Hou et al., 2024) and delivers IL-10 mRNA to promote osteogenic differentiation while inhibiting osteoclastic differentiation (Chen et al., 2022). hucMSC-EV, on the one hand, promotes osteogenic differentiation of human periodontal ligament stem cells (hPDLSCs) under high glucose conditions via the PI3K/AKT signalling pathway (Yang et al., 2022); on the other hand, by delivering miR-2110, it targets TNF-α to negatively regulate the bone absorption activity of osteoclasts (Yahao & Xinjia, 2021). Furthermore, fEV may indirectly promote bone metabolic homeostasis by inhibiting macrophage pyroptosis. hucMSC-EV negatively regulates NLRP3 inflammasome activation by enriching miR-100-5p, miR-26a-5p, miR-203a-3p and miR-378a-5p (Cai et al., 2021; Liang et al., 2020; Xu et al., 2022; Yuan et al., 2021). The overexpression of miR-30b-5p in M_2-EV is closely associated with the inhibition of miR-148a and cell pyroptosis (Dai et al., 2020; Tang et al., 2022). We also analysed miRNA expression in M_2-EV and hucMSC-EV using an existing GEO dataset (GSE155745 and GSE159814). We found that each expression spectrum has its unique miRNA, some of the miRNA mentioned above were specific expressions in each EVs (miR-365-2-5 in M_2-EV and miR-203a-3p, miR-2110 in hucMSC-EV), the intersection of these expression spectrums is not the major part (Figure S9). Among the top 9 miRNAs with the highest proportion (52.4%) of expression levels in hucMSC-EV (miR-21-5p, miR-24-3p, miR-22-3p, miR-26a-5p, miR-146a-5p, miR-221-3p, let-7a-5p, miR-29a-3p and miR-100-5p), they exhibited the ability to inhibit osteoclast, pyroptosis, anti-inflammation. In summary, fEV potentially regulates macrophage pyroptosis and bone metabolic homeostasis induced by wear particles through multiple pathways and mechanisms. Nonetheless, the specific molecular targets of fEV action warrant further investigation.

In this study, we proposed and successfully developed a fusion EV platform for delivering hucMSC-EV via M_2-EV, addressing the challenge of targeted hucMSC-EV delivery in vivo. The application of fEV demonstrated promising results in targeted prevention and treatment of wear particle-induced osteolysis around prostheses, yielding several original findings. However, our work has certain limitations. We used LPS (component of the outer wall of Gram-negative bacterial cell walls) to induce the transcription of NLRP3, to stimulate pyroptosis model in vitro, while Xue et al. (2022) treated BMDM with TNF-α (endogenous cytokines) to trigger this process. We will continue to delve deeper into the biological mechanisms of pyroptosis to find a better model to simulate this sterile inflammatory response. Prior studies have outlined various technical methods for achieving membrane fusion based on the phospholipid bilayer structure, including the ultrasonic heating method (Xiong et al., 2021), the heating stirring method (Dehaini et al., 2017) and the liposome extrusion method utilized in this study. It is imperative to further explore alternative fusion approaches and assess their efficiency. Additionally, to ascertain the preservation of fEV's biological function and elucidate its precise molecular targets, we plan to conduct transcriptomic or proteomic analyses of M_2-EV, hucMSC-EV and fEV, along with their target cells, and establish a miRNA-transcriptomic negative regulatory network. This will enable us to validate the retention of therapeutic biomolecules within fEV and unravel the exact molecular mechanisms underlying its action. Furthermore, several challenges must be addressed before the clinical application of fEV can be realized: (1) verification of fEV's efficacy in preventing and treating prosthesis loosening in humans remains crucial; (2) consideration of immune rejection and ethical concerns associated with individual fEV application; (3) assessment of the long-term safety of fEV in vivo; (4) development of standardized preparation protocols and quality inspection processes for fEV, as well as strategies to reduce application costs; and (5) design considerations for artificial joint prostheses incorporating biological coatings enriched with fEV. Addressing these issues will pave the way for the clinical implementation of fEV, offering novel insights into the application of sEVs in medical practice.

AUTHOR CONTRIBUTIONS

Qimeng Liu: Investigation (lead); methodology (lead); and writing—original draft (lead). Tianliang Ma: Writing—original draft (equal) and writing—review and editing (equal). Zheyu Zhang: Data curation (equal) and methodology (equal). Jiangyu Nan: Investigation (equal) and methodology (equal). Guanzhi Liu: Data curation (equal) and software (equal). Yute Yang: Data curation (equal) and software (equal). Yihe Hu: Funding acquisition (equal). Jie Xie: Funding acquisition (lead) and writing—review and editing (equal). Qimeng Liu and Tianliang Ma contributed equally to this study.

ACKNOWLEDGEMENTS

This work was supported by the National Natural Science Foundation of China under grant numbers 82272452, 82372414 and 82202733 and the Zhejiang Provincial Natural Science Foundation of China under grant number Y24H060021. Graph abstract was created with BioRender.com. The authors extend their gratitude to Ms. Ma from Shiyanjia Lab (www.shiyanjia.com) for providing invaluable assistance with the TEM.

CONFLICT OF INTEREST STATEMENT

The authors declare no conflicts of interest.

DATA AVAILABILITY STATEMENT

The data underlying this study will be shared on reasonable request to the corresponding author.

ORCID

Jie Xie https://orcid.org/0000-0001-8042-0600

REFERENCES

Alhasan, H., Terkawi, M. A., Matsumae, G., Ebata, T., Tian, Y., Shimizu, T., Nishida, Y., Yokota, S., Garcia-Martin, F., M Abd Elwakil, M., Takahashi, D., Younis, M. A., Harashima, H., Kadoya, K., & Iwasaki, N. (2022). Inhibitory role of Annexin A1 in pathological bone resorption and therapeutic implications in periprosthetic osteolysis. *Nature Communications*, *13*, 3919.

An, S., Han, F., Hu, Y., Liu, Y., Li, J., & Wang, L. (2018). Curcumin inhibits polyethylene-induced osteolysis via repressing NF-kappaB signaling pathway activation. *Cellular Physiology and Biochemistry: International Journal of Experimental Cellular Physiology, Biochemistry, and Pharmacology*, *50*, 1100–1112.

Buckley, C. D., Gilroy, D. W., & Serhan, C. N. (2014). Proresolving lipid mediators and mechanisms in the resolution of acute inflammation. *Immunity*, *40*, 315–327.

Burton, L., Paget, D., Binder, N. B., Bohnert, K., Nestor, B. J., Sculco, T. P., Santambrogio, L., Ross, F. P., Goldring, S. R., & Purdue, P. E. (2013). Orthopedic wear debris mediated inflammatory osteolysis is mediated in part by NALP3 inflammasome activation. *Journal of Orthopaedic Research*, *31*, 73–80.

Cai, X., Zhang, Z. Y., Yuan, J. T., Ocansey, D. K. W., Tu, Q., Zhang, X., Qian, H., Xu, W. R., Qiu, W., & Mao, F. (2021). hucMSC-derived exosomes attenuate colitis by regulating macrophage pyroptosis via the miR-378a-5p/NLRP3 axis. *Stem Cell Research & Therapy*, *12*, 416.

Cao, H., Dan, Z., He, X., Zhang, Z., Yu, H., Yin, Q., & Li, Y. (2016). Liposomes coated with isolated macrophage membrane can target lung metastasis of breast cancer. *ACS Nano*, *10*, 7738–7748.

Chen, W., Sun, Y., Gu, X., Cai, J., Liu, X., Zhang, X., Chen, J., Hao, Y., & Chen, S. (2021). Conditioned medium of human bone marrow-derived stem cells promotes tendon-bone healing of the rotator cuff in a rat model. *Biomaterials*, *271*, 120714.

Chen, X., Wan, Z., Yang, L., Song, S., Fu, Z., Tang, K., Chen, L., & Song, Y. (2022). Exosomes derived from reparative M2-like macrophages prevent bone loss in murine periodontitis models via IL-10 mRNA. *Journal of Nanobiotechnology*, *20*, 110.

Chen, Z. S., Luo, L., Ye, T., Zhou, J. C., Niu, X., Yuan, J., Yuan, T., Fu, D. H., Li, H. Y., Li, Q., & Wang, Y. (2024). Identification of specific markers for human pluripotent stem cell-derived small extracellular vesicles. *Journal of Extracellular Vesicles*, *13*(2), e12409.

Cobelli, N., Scharf, B., Crisi, G. M., Hardin, J., & Santambrogio, L. (2011). Mediators of the inflammatory response to joint replacement devices. *Nature Reviews Rheumatology*, *7*, 600–608.

Conos, S. A., Chen, K. W., De Nardo, D., Hara, H., Whitehead, L., Nunez, G., Masters, S. L., Murphy, J. M., Schroder, K., Vaux, D. L., Lawlor, K. E., Lindqvist, L. M., & Vince, J. E. (2017). Active MLKL triggers the NLRP3 inflammasome in a cell-intrinsic manner. *PNAS*, *114*, E961–E969.

Dai, Y., Wang, S., Chang, S., Ren, D., Shali, S., Li, C., Yang, H., Huang, Z., & Ge, J. (2020). M2 macrophage-derived exosomes carry microRNA-148a to alleviate myocardial ischemia/reperfusion injury via inhibiting TXNIP and the TLR4/NF-kappaB/NLRP3 inflammasome signaling pathway. *Journal of Molecular and Cellular Cardiology*, *142*, 65–79.

Dehaini, D., Wei, X., Fang, R. H., Masson, S., Angsantikul, P., Luk, B. T., Zhang, Y., Ying, M., Jiang, Y., Kroll, A. V., Gao, W., & Zhang, L. (2017). Erythrocyte-platelet hybrid membrane coating for enhanced nanoparticle functionalization. *Advanced Materials*, *29*(16), 10.1002.

Dong, J., Zhang, L., Ruan, B., Lv, Z., Wang, H., Wang, Y., Jiang, Q., & Cao, W. (2022). NRF2 is a critical regulator and therapeutic target of metal implant particle-incurred bone damage. *Biomaterials*, *288*, 121742.

Dong, L., Pu, Y., Zhang, L., Qi, Q., Xu, L., Li, W., Wei, C., Wang, X., Zhou, S., Zhu, J., Wang, X., Liu, F., Chen, X., & Su, C. (2018). Human umbilical cord mesenchymal stem cell-derived extracellular vesicles promote lung adenocarcinoma growth by transferring miR-410. *Cell Death & Disease*, *9*, 218.

Drees, P., Eckardt, A., Gay, R. E., Gay, S., & Huber, L. C. (2007). Mechanisms of disease: Molecular insights into aseptic loosening of orthopedic implants. *Nature Clinical Practice Rheumatology*, *3*, 165–171.

Edwards, J. R., & Mundy, G. R. (2011). Advances in osteoclast biology: Old findings and new insights from mouse models. *Nature Reviews Rheumatology*, *7*, 235–243.

Fullerton, J. N., & Gilroy, D. W. (2016). Resolution of inflammation: A new therapeutic frontier. *Nat Rev Drug Discovery*, *15*, 551–567.

Gallo, J., Vaculova, J., Goodman, S. B., Konttinen, Y. T., & Thyssen, J. P. (2014). Contributions of human tissue analysis to understanding the mechanisms of loosening and osteolysis in total hip replacement. *Acta Biomaterialia*, *10*, 2354–2366.

Goodman, S. B., & Gallo, J. (2019). Periprosthetic osteolysis: Mechanisms, prevention and treatment. *Journal of Clinical Medicine*, *8*, 2091.

He, C., Zheng, S., Luo, Y., & Wang, B. (2018). Exosome theranostics: Biology and translational medicine. *Theranostics*, *8*, 237–255.

Hodges, N. A., Sussman, E. M., & Stegemann, J. P. (2021). Aseptic and septic prosthetic joint loosening: Impact of biomaterial wear on immune cell function, inflammation, and infection. *Biomaterials*, *278*, 121127.

Hou, C., Zhang, Y., Lv, Z., Luan, Y., Li, J., Meng, C., Liu, K., Luo, X., Chen, L., & Liu, F. (2024). Macrophage exosomes modified by miR-365-2-5p promoted osteoblast osteogenic differentiation by targeting OLFML1. *Regen Biomater*, *11*, rbae018.

Hu, S., Wang, X., Li, Z., Zhu, D., Cores, J., Wang, Z., Li, J., Mei, X., Cheng, X., Su, T., & Cheng, K. (2021). Platelet membrane and stem cell exosome hybrid enhances cellular uptake and targeting to heart injury. *Nano Today*, *39*, 101210.

Hua, T., Yang, M., Song, H., Kong, E., Deng, M., Li, Y., Li, J., Liu, Z., Fu, H., Wang, Y., & Yuan, H. (2022). Huc-MSCs-derived exosomes attenuate inflammatory pain by regulating microglia pyroptosis and autophagy via the miR-146a-5p/TRAF6 axis. *Journal of nanobiotechnology*, *20*, 324.

Huang, R., Zhang, L., Li, X., Liu, F., Cheng, X., Ran, H., Wang, Z., Li, Y., Feng, Y., Liang, L., Su, W., Melgiri, N. D., & Sun, Y. (2023). Anti-CXCR2 antibody-coated nanoparticles with an erythrocyte-platelet hybrid membrane layer for atherosclerosis therapy. *Journal of Controlled Release*, *356*, 610–622.

Kim, J. H., Jin, H. M., Kim, K., Song, I., Youn, B. U., Matsuo, K., & Kim, N. (2009). The mechanism of osteoclast differentiation induced by IL-1. *Journal of Immunology*, *183*, 1862–1870.

Kim, M. S., Haney, M. J., Zhao, Y., Mahajan, V., Deygen, I., Klyachko, N. L., Inskoe, E., Piroyan, A., Sokolsky, M., Okolie, O., Hingtgen, S. D., Kabanov, A. V., & Batrakova, E. V. (2016). Development of exosome-encapsulated paclitaxel to overcome MDR in cancer cells. *Nanomedicine*, *12*(3), 655–664.

Lee, N. K., Choi, Y. G., Baik, J. Y., Han, S. Y., Jeong, D. W., Bae, Y. S., Kim, N., & Lee, S. Y. (2005). A crucial role for reactive oxygen species in RANKL-induced osteoclast differentiation. *Blood*, *106*, 852–859.

Li, L., He, D., Guo, Q., Zhang, Z., Ru, D., Wang, L., Gong, K., Liu, F., Duan, Y., & Li, H. (2022a). Exosome-liposome hybrid nanoparticle codelivery of TP and miR497 conspicuously overcomes chemoresistant ovarian cancer. *Journal of Nanobiotechnology*, *20*, 50.

Li, Q., Huang, Z., Wang, Q., Gao, J., Chen, J., Tan, H., Li, S., Wang, Z., Weng, X., Yang, H., Pang, Z., Song, Y., Qian, J., & Ge, J. (2022b). Targeted immunomodulation therapy for cardiac repair by platelet membrane engineering extracellular vesicles via hitching peripheral monocytes. *Biomaterials*, *284*, 121529.

Li, R., He, Y., Zhu, Y., Jiang, L., Zhang, S., Qin, J., Wu, Q., Dai, W., Shen, S., Pang, Z., & Wang, J. (2019). Route to rheumatoid arthritis by macrophage-derived microvesicle-coated nanoparticles. *Nano Letters*, *19*, 124–134.

Liang, C., Liu, Y., Xu, H., Huang, J., Shen, Y., Chen, F., & Luo, M. (2020). Exosomes of human umbilical cord MSCs protect against hypoxia/reoxygenation-induced pyroptosis of cardiomyocytes via the miRNA-100-5p/FOXO3/NLRP3 pathway. *Frontiers in Bioengineering and Biotechnology*, *8*, 615850.

Lu, T. X., & Rothenberg, M. E. (2018). MicroRNA. *Journal of Allergy and Clinical Immunology*, *141*, 1202–1207.

Pan, B., Zhang, Z., Wu, X., Xian, G., Hu, X., Gu, M., Zheng, L., Li, X., Long, L., Chen, W., & Sheng, P. (2023). Macrophage-derived exosomes modulate wear particle-induced osteolysis via miR-3470b targeting TAB3/NF-kappaB signaling. *Bioactive Materials*, *26*, 181–193.

Panez-Toro, I., Heymann, D., Gouin, F., Amiaud, J., Heymann, M. F., & Cordova, L. A. (2023). Roles of inflammatory cell infiltrate in periprosthetic osteolysis. *Frontiers in Immunology*, *14*, 1310262.

Rayamajhi, S., Nguyen, T. D. T., Marasini, R., & Aryal, S. (2019). Macrophage-derived exosome-mimetic hybrid vesicles for tumor targeted drug delivery. *Acta Biomaterialia*, *94*, 482–494.

Saari, H., Lazaro-Ibanez, E., Viitala, T., Vuorimaa-Laukkanen, E., Siljander, P., & Yliperttula, M. (2015). Microvesicle- and exosome-mediated drug delivery enhances the cytotoxicity of Paclitaxel in autologous prostate cancer cells. *Journal of Controlled Release*, *220*, 727–737.

Shi, J., Zhao, Y., Wang, Y., Gao, W., Ding, J., Li, P., Hu, L., & Shao, F. (2014). Inflammatory caspases are innate immune receptors for intracellular LPS. *Nature*, *514*, 187–192.

Son, H. S., Lee, J., Lee, H. I., Kim, N., Jo, Y. J., Lee, G. R., Hong, S. E., Kwon, M., Kim, N. Y., Kim, H. J., Park, J. H., Lee, S. Y., & Jeong, W. (2020a). Benzydamine inhibits osteoclast differentiation and bone resorption via down-regulation of interleukin-1 beta expression. *Acta Pharmaceutica Sinica B*, *10*, 462–474.

Szmukler-Moncler, S., Salama, H., Reingewirtz, Y., & Dubruille, J. H. (1998). Timing of loading and effect of micromotion on bone-dental implant interface: Review of experimental literature. *Journal of Biomedial Materials Research*, *43*, 192–203.

Tang, B., Wu, Y., Zhang, Y., Cheng, Y., Wu, Y., & Fang, H. (2022). Scorpion and centipede alleviates severe asthma through M2 macrophage-derived exosomal miR-30b-5p. *Aging (Albany NY)*, *14*, 3921–3940.

Tang, J. N., Su, T., Huang, K., Dinh, P. U., Wang, Z. G., Vandergriff, A., Hensley, M. T., Cores, J., Allen, T., Li, T. S., Sproul, E., Mihalko, E., Lobo, L. J., Ruterbories, L., Lynch, A., Brown, A., Caranasos, T. G., Shen, D., Stouffer, G. A., … Cheng, K. (2018). Targeted repair of heart injury by stem cells fused with platelet nanovesicles. *Nature Biomedical Engineering*, *2*, 17–26.

Tschopp, J., & Schroder, K. (2010). NLRP3 inflammasome activation: The convergence of multiple signalling pathways on ROS production? *Nature Reviews Immunology*, *10*, 210–215.

Wang, H., Wu, J., Williams, G. R., Fan, Q., Niu, S., Wu, J., Xie, X., & Zhu, L. M. (2019). Platelet-membrane-biomimetic nanoparticles for targeted antitumor drug delivery. *Journal of Nanobiotechnology*, *17*, 60.

Wang, L., Wang, J., Zhou, X., Sun, J., Zhu, B., Duan, C., Chen, P., Guo, X., Zhang, T., & Guo, H. (2020). A new self-healing hydrogel containing hucMSC-derived exosomes promotes bone regeneration. *Frontiers in Bioengineering and Biotechnology*, *8*, 564731.

Wei, Z., Hang, S., Wiredu Ocansey, D. K., Zhang, Z., Wang, B., Zhang, X., & Mao, F. (2023). Human umbilical cord mesenchymal stem cells derived exosome shuttling mir-129-5p attenuates inflammatory bowel disease by inhibiting ferroptosis. *Journal of Nanobiotechnology*, *21*, 188.

Weischenfeldt, J., & Porse, B. (2008). Bone marrow-derived macrophages (BMM): Isolation and applications. *Cold Spring Harbor Protocols*, pdb prot5080.

Wu, S., Yun, J., Tang, W., Familiari, G., Relucenti, M., Wu, J., Li, X., Chen, H., & Chen, R. (2023). Therapeutic m(6)A eraser ALKBH5 mRNA-loaded exosome-liposome hybrid nanoparticles inhibit progression of colorectal cancer in preclinical tumor models. *ACS Nano*, *17*, 11838–11854.

Wu, Y., Teng, Y., Zhang, C., Pan, Y., Zhang, Q., Zhu, X., Liu, N., Su, X., & Lin, J. (2022a). The ketone body beta-hydroxybutyrate alleviates CoCrMo alloy particles induced osteolysis by regulating NLRP3 inflammasome and osteoclast differentiation. *Journal of Nanobiotechnology*, *20*, 120.

Wu, Y., Wan, S., Yang, S., Hu, H., Zhang, C., Lai, J., Zhou, J., Chen, W., Tang, X., Luo, J., Zhou, X., Yu, L., Wang, L., Wu, A., Fan, Q., & Wu, J. (2022b). Macrophage cell membrane-based nanoparticles: A new promising biomimetic platform for targeted delivery and treatment. *Journal of Nanobiotechnology*, *20*, 542.

Wu, Y. L., Zhang, C. H., Teng, Y., Pan, Y., Liu, N. C., Liu, P. X., Zhu, X., Su, X. L., & Lin, J. (2022c). Propionate and butyrate attenuate macrophage pyroptosis and osteoclastogenesis induced by CoCrMo alloy particles. *Military Medical Research*, *9*, 46.

Wynn, T. A., Chawla, A., & Pollard, J. W. (2013). Macrophage biology in development, homeostasis and disease. *Nature*, *496*, 445–455.

Xiong, J., Wu, M., Chen, J., Liu, Y., Chen, Y., Fan, G., Liu, Y., Cheng, J., Wang, Z., Wang, S., Liu, Y., & Zhang, W. (2021). Cancer-erythrocyte hybrid membrane-camouflaged magnetic nanoparticles with enhanced photothermal-immunotherapy for ovarian cancer. *ACS Nano*, *15*, 19756–19770.

Xu, Y., Tang, X., Fang, A., Yan, J., Kofi Wiredu Ocansey, D., Zhang, X., & Mao, F. (2022). HucMSC-Ex carrying miR-203a-3p.2 ameliorates colitis through the suppression of caspase11/4-induced macrophage pyroptosis. *International Immunopharmacology*, *110*, 108925.

Xue, S., Xu, Y., Xu, S., Zhong, Y., Ruan, G., Ma, J., Hu, Y., Ding, C., & Sang, W. (2022). Mitophagy impairment mediates the pathogenesis of CoCrMo particle-induced osteolysis via NLRP3/caspase-1/GSDMD-dependent pyroptosis in macrophages. *Chemical Engineering Journal*, 435.

Yahao, G., & Xinjia, W. (2021). The role and mechanism of exosomes from umbilical cord mesenchymal stem cells in inducing osteogenesis and preventing osteoporosis. *Cell Transplantation*, *30*, 9636897211057465.

Yan, B., Zhang, Y., Liang, C., Liu, B., Ding, F., Wang, Y., Zhu, B., Zhao, R., Yu, X. Y., & Li, Y. (2020). Stem cell-derived exosomes prevent pyroptosis and repair ischemic muscle injury through a novel exosome/circHIPK3/FOXO3a pathway. *Theranostics*, *10*, 6728–6742.

Yang, S., Zhu, B., Tian, X. Y., Yu, H. Y., Qiao, B., Zhao, L. S., & Zhang, B. (2022). Exosomes derived from human umbilical cord mesenchymal stem cells enhance the osteoblastic differentiation of periodontal ligament stem cells under high glucose conditions through the PI3K/AKT signaling pathway. *Biomedical and Environmental Sciences*, *35*, 811–820.

Yim, K. H. W., Krzyzaniak, O., Al Hrout, A., Peacock, B., & Chahwan, R. (2023). Assessing extracellular vesicles in human biofluids using flow-based analyzers. *Advanced Healthcare Materials*, *12*, 10.

Yin, W., Liu, S., Dong, M., Liu, Q., Shi, C., Bai, H., Wang, Q., Yang, X., Niu, W., & Wang, L. (2020). A new NLRP3 Inflammasome inhibitor, dioscin, promotes osteogenesis. *Small*, *16*, e1905977.

Ying, W., Gao, H., Dos Reis, F. C. G., Bandyopadhyay, G., Ofrecio, J. M., Luo, Z., Ji, Y., Jin, Z., Ly, C., & Olefsky, J. M. (2021). MiR-690, an exosomal-derived miRNA from M2-polarized macrophages, improves insulin sensitivity in obese mice. *Cell Metabolism*, *33*, 781–790e785.

Ying, W., Riopel, M., Bandyopadhyay, G., Dong, Y., Birmingham, A., Seo, J. B., Ofrecio, J. M., Wollam, J., Hernandez-Carretero, A., Fu, W., Li, P., & Olefsky, J. M. (2017). Adipose tissue macrophage-derived exosomal miRNAs can modulate in vivo and in vitro insulin sensitivity. *Cell*, *171*, 372–384e312.

Yuan, X., Li, T., Shi, L., Miao, J., Guo, Y., & Chen, Y. (2021). Human umbilical cord mesenchymal stem cells deliver exogenous miR-26a-5p via exosomes to inhibit nucleus pulposus cell pyroptosis through METTL14/NLRP3. *Molecular Medicine*, *27*, 91.

Zaveri, T. D., Dolgova, N. V., Lewis, J. S., Hamaker, K., Clare-Salzler, M. J., & Keselowsky, B. G. (2017). Macrophage integrins modulate response to ultra-high molecular weight polyethylene particles and direct particle-induced osteolysis. *Biomaterials*, *115*, 128–140.

Zhu, S., Ding, S., Wang, P., Wei, Z., Pan, W., Palm, N. W., Yang, Y., Yu, H., Li, H. B., Wang, G., Lei, X., de Zoete, M. R., Zhao, J., Zheng, Y., Chen, H., Zhao, Y., Jurado, K. A., Feng, N., Shan, L., … Flavell, R. A. (2017). Nlrp9b inflammasome restricts rotavirus infection in intestinal epithelial cells. *Nature*, *546*, 667–670.

SUPPORTING INFORMATION

Additional supporting information can be found online in the Supporting Information section at the end of this article.

How to cite this article: Liu, Q., Ma, T., Zhang, Z., Nan, J., Liu, G., Yang, Y., Hu, Y., & Xie, J. (2024). Fused extracellular vesicles from M_2 macrophages and human umbilical cord mesenchymal stem cells for the targeted regulation of macrophage pyroptosis in periprosthetic osteolysis. *Journal of Extracellular Vesicles*, *13*, e70028. https://doi.org/10.1002/jev2.70028